EUROPEAN ORGANIZATION FOR NUCLEAR RESEARCH

CERN-EP/85-115
22 July 1985

A SEARCH FOR GLUEBALLS AND A STUDY OF DOUBLE POMERON EXCHANGE AT THE CERN INTERSECTING STORAGE RINGS

(The Axial Field Spectrometer Collaboration)

T. Åkesson[4], M.G. Albrow[10], S. Almehed[6], R. Batley[4], O. Benary[11], H. Bøggild[5], O. Botner[5], H. Breuker[4], V. Burkert[2], R. Carosi[4], A.A. Carter[9], J.R. Carter[3], P.C. Cecil[3], S.U. Chung[1], W.E. Cleland[8], D. Cockerill[10], S. Dagan[11], E. Dahl-Jensen[5], I. Dahl-Jensen[5], P. Dam[5], G. Damgaard[5], W.M. Evans[10], C.W. Fabjan[4], P. Frandsen[4], S. Frankel[7], W. Frati[7], M.D. Gibson[10], U. Goerlach[4], M.J. Goodrick[3], K.H. Hansen[5], V. Hedberg[6], J.W. Hiddleston[10], H.J. Hilke[4], G. Jarlskog[6], T. Killian[1], R. Kroeger[8], K. Kulka[6], J. v.d. Lans[4], J. Lindsay[4], D. Lissauer[11], B. Lörstad[6], T. Ludlam[1], A. Markou[4], N.A. McCubbin[10], U. Mjörnmark[6], R. Møller[5], W. Molzon[7], B.S. Nielsen[4], A. Nilsson[6], L.H. Olsen[4], Y. Oren[11], T.W. Pritchard[9], L. Rosselet[4], E. Rosso [4], A. Rudge[4], I. Stumer[1], M. Sullivan[8], J.A. Thompson[8], G. Thorstenson[6], E. Vella[7], D. Weygand[1], J.G. Williamson[10], W.J. Willis[4], M. Winik[1], W. Witzeling[4], C. Woody[1] and W.A. Zajc[7]

(Submitted to Nuclear Physics B)

---

1 Brookhaven National Laboratory, Upton, NY, USA
2 Physikalisches Institut, Universität Bonn, Fed. Rep. Germany
3 Cambridge University, Cambridge, UK
4 CERN, Geneva, Switzerland
5 Niels Bohr Institute, Copenhagen, Denmark
6 University of Lund, Sweden
7 University of Pennsylvania, Philadelphia, PA, USA
8 University of Pittsburgh, Pittsburgh, PA, USA
9 Queen Mary College, London, UK
10 Rutherford Appleton Laboratory, Didcot, UK
11 University of Tel Aviv, Israel

ABSTRACT

We present results from a study of centrally produced mesons in 3×10^6 events with two small-angle protons at the CERN Intersecting Storage Rings. A high-statistics sample of exclusive $pp \to pp\pi^+\pi^-$ events at $\sqrt{s} = 63$ GeV has been obtained, where the reaction mechanism is dominated by double pomeron exchange. Scalar or tensor glueballs may be produced by this process. The $\pi^+\pi^-$ mass spectrum has a distinctive structure, and analysis shows that the data are dominantly S-wave up to 1600 MeV. The behaviour of the D-wave provides evidence for a 2^{++} resonance ($M = 1480 \pm 50$ MeV, $\Gamma = 150 \pm 50$ MeV) in addition to the f(1270). We also show data on exclusive K^+K^-, $p\bar{p}$, and $\pi^+\pi^-\pi^+\pi^-$ production, and on the analogous reaction $\alpha\alpha \to \alpha\alpha\pi^+\pi^-$ at $\sqrt{s} = 126$ GeV. Flavour independence is suggested by the observation of approximately equal numbers of K^+K^- and $\pi^+\pi^-$ pairs for mass above 1 GeV. The mass spectra are also apparently independent of $\sqrt{s}$ (45, 63, 126 GeV) and incident particle type (p, α).

1. INTRODUCTION

We present results from a study of centrally produced systems of charged particles at the CERN Intersecting Storage Rings (ISR). The major part of this analysis is concerned with the exclusive reaction $pp \to p\pi^+\pi^- p$ at $\sqrt{s} = 63$ GeV, where the two protons are scattered by typically 5 mrad, losing little of their initial c.m. momenta, and have $0.01 \lesssim |t| \lesssim 0.06\ \text{GeV}^2$, $x_F \geq 0.95$, and $|y| \sim 4.2$. The central system is well isolated in rapidity. This final sample represents a factor of 3 increase in statistics over our previously published data [1]. Also, a more complete study of the detector acceptance has now permitted a partial-wave analysis of the $\pi^+\pi^-$ system.

The state X^0 produced via the exclusive process $pp \to pX^0p$ must have $Q = B = S = 0$. For the kinematical ranges outlined above the process is dominated by double pomeron exchange (DPE) [2], and X^0 is constrained to have $I = 0$, $G = +1$, $C = +1$, with $J = 0, 2, 4$, etc. This provides a powerful tool for meson spectroscopy. The isolation of a clean DPE signal has only been possible at the highest ISR energy [3]. Evidence for non-DPE is a ϱ^0 signal in the $\pi^+\pi^-$ channel, seen in experiments at lower c.m. energies [4].

In QCD, the pomeron is generally considered to be multiple gluon exchange, and, as was first pointed out by Robson [5], DPE should favour the production of glueballs. The bag model [6] predicts ground-state scalar and tensor two-gluon glueballs at around 1.0 and 1.3 GeV respectively. Many authors have suggested [7] that mixing with ordinary $q\bar{q}$ mesons will occur [e.g. the 0^{++} with S* (980) and the 2^{++} with f(1270)]. Experimental candidates exist in the scalar G(1590) claimed in $\pi^- p \to \eta\eta n$ [8], and the tensor $\theta(1700)$ seen in $\eta\eta$, $K\bar{K}$ and probably $\pi\pi$ channels in radiative J/ψ decay [9, 10]. Three broad 2^{++} states have also been reported in the $\phi\phi$ channel in $\pi^- p \to \phi\phi n$ [11].

In the following section we describe our apparatus and data-acquisition techniques, and the analysis is discussed in detail in Section 3. The results for $\pi^+\pi^-$ exclusive events are presented in Section 4, including the angular distributions and partial-wave analysis. Other exclusive channels are described in Section 5. Finally, in Section 6 we give evidence for the observation of exclusive $\alpha\alpha \to \alpha\pi^+\pi^-\alpha$ events.

2. APPARATUS AND DATA ACQUISITION

The Axial Field Spectrometer (AFS) has been described in detail elsewhere [12]. Figure 1 shows the schematic layout of the detectors used in this analysis. The axial field magnet (AFM) produced a field of about 0.5 T in the central region. The central cylindrical drift chamber was 1.6 m in diameter and 1.5 m long, and was divided in the vertical plane. The azimuthal coverage achieved was over 85% (there being dead regions above and below due to beam-pipe supports). The sense wires were arranged in 82 sectors, each of 4° in azimuth ϕ, and in 3 crowns in radius R, of 14, 18, and 10 wires, respectively. The ambiguity within a sector was resolved by staggering alternate wires by ± 0.4 mm.

Charged particles were measured with up to 42 space points per track, with $\Delta p_T/p_T \approx 2\%\ p_T$ (GeV). The coordinates in the axial (z) direction were determined by the charge division technique, with an average resolution of $\sigma = 1.5$ cm. The chamber also provided particle identification by dE/dx in the non-relativistic region. Surrounding the ISR beam pipe was a 44-element 'barrel' scintillator hodoscope, used for triggering purposes.

The trajectories of the forward protons were measured by small drift chambers located ~ 9 m from the intersection region above (UP) and below (DOWN) each downstream beam pipe (see Fig. 1). The drift chambers (described in Ref. [13]) had four horizontal sense wires. The vertical coordinate was measured by drift-time with a precision of $\sigma \approx 120\ \mu$m per wire, and charge division gave the horizontal coordinate to $\sigma \approx 1.2$ mm. After passing through the ISR vacuum chamber for ~ 8.2 m, each forward proton emerged through a 0.2 mm thick stainless-steel window in a transition from a circular to an elliptical

beam-pipe section. Multiple scattering and angular deflections due to magnetic fields were negligible, and the vertical and horizontal angles were measured with $\sigma \approx 0.09$ mrad and 0.3 mrad, respectively. Each forward arm covered $3 \lesssim \theta \lesssim 8$ mrad over $\sim 45°$ of azimuth. Two 30 mm $\times$ 30 mm scintillators at the front and back of each telescope were used for triggering purposes. Most of the medium-angle region was covered by about 100 scintillation counters, providing a veto for charged particles in $1.5 \lesssim |y| \lesssim 3.0$. These counters were preceded by 1 radiation length of lead to have some efficiency for counting π^0's.

The trigger required a coincidence of the following conditions:

i) A coincidence between the two scintillators in both 'UP' arms or both 'DOWN' arms (thus eliminating background from elastic scattering).

ii) At least two elements of the central 'barrel' hodoscope to have hits.

iii) No particles detected by the veto counters.

The data were acquired continuously over the last 15 months of colliding-beam operation at the ISR, and amounted to 3 million triggered events. The 'very fast bus' (VFB) parallel-trigger processor [14] enabled this to be done in parallel with the other AFS data taking, with an overall live-time of about 70%.

3. DATA REDUCTION AND ANALYSIS

The standard AFS pattern-recognition and track-fitting programs were used to reconstruct the central tracks in each event. Basic quality cuts were applied to the track and vertex fits, to eliminate badly measured events. For the present analysis events were selected with just 2 or 4 central tracks fitting to a common vertex. The trigger geometry implies that exclusive events should have a central system recoiling against the forward protons. This is illustrated in Fig. 2, where the resultant vertical (y) momentum of the central tracks has been plotted. For $Q = 0$ systems clear peaks are visible at $+0.32$ GeV/c (for (DOWN–DOWN) and -0.32 GeV/c (for UP–UP). Applying momentum balance, the mean vertical angle of the forward tracks of 5.5 mrad implies a scattered proton momentum of approximately $0.5 \times 0.32/0.0055 \approx 30$ GeV/c, as expected. No corresponding peaks are observed for $Q \neq 0$ systems (lower histograms of Fig. 2), and these events were rejected.

The central tracks were identified using the truncated mean of the dE/dx measurements (see Fig. 3), classifying them as unambiguous π, K or p($\bar{p}$), ambiguous π/K, or ambiguous π/K/p($\bar{p}$). For events with two central particles only one of the tracks needed to be identified unambiguously, with the other consistent with having the same identity. If both tracks were ambiguous, then a $\pi^+\pi^-$ event was assumed.

Straight tracks were fitted to the forward drift-chamber coordinates, giving the angles of the scattered protons at the vertex. Owing to small displacements caused by the AFM and beam compensator magnets the dy/dz (vertical slope) fit used only the forward-arm information, whereas for dx/dz (horizontal slope) the main vertex position could be included in the fit (x, y, and z are defined in Fig 1). The proton momenta were then calculated, assuming an exclusive event, using the energy and longitudinal momentum (p_z) constraints. For this calculation the incident beam momenta were corrected for momentum compaction (i.e. the correlation between momentum and position in the beam) using the measured vertex position. The distribution of Σp_y for all final-state particles (forward + central) is centred at zero with $\sigma = 30$ MeV/c (Fig. 4a). A cut was applied at ± 80 MeV/c. The difference between Σp_x of the initial and final states (Fig. 4b) is peaked strongly at zero and a cut was applied at ± 100 MeV/c. The final exclusive sample consists of 89,000 events, and we estimate from extrapolation of the distributions outside the cuts that the residual non-exclusive background is $\sim 5\%$. Most (97%) of the events were classified as $\pi^+\pi^-$, and of these only 6% have ambiguous identification for both particles. A full two-constraint fit, applied to a subset of the data, gave similar results to the simplified exclusive cuts described above. The Feynman x of the forward protons peaks at $x \sim 0.99$, and 95% of the events have $x > 0.95$.

4. THE $\pi^+\pi^-$ EXCLUSIVE EVENTS

4.1 The effective mass distribution

The effective mass of the $\pi^+\pi^-$ events is shown on a logarithmic scale in Fig. 5 in 25 MeV bins. No correction for acceptance has been made at this stage. The mass resolution changes from 10 MeV at 1 GeV to 25 MeV at 2 GeV, and there is no evidence for a systematic shift in the mass scale. [Another AFS study found $M(J/\psi) = 3097 \pm 12$ MeV]. The detail of the low-mass region is shown in Fig. 6a, in 10 MeV bins. The distribution rises rapidly from threshold, peaks at about 500 MeV, and then falls smoothly until 950 MeV. There is no significant enhancement at the ϱ^0 mass (770 MeV), showing that there is little background from non-pomeron exchange.

The distribution drops by an order of magnitude between 950 and 1050 MeV. The higher mass regions are shown in detail in Fig. 6b and c. There is a broad enhancement centred at 1300 MeV, but no characteristic signal for the f(1270). There is another relatively rapid drop between 1400 and 1600 MeV, followed by a broad continuum structure which again decreases relatively rapidly at around 2300 MeV.

We increased the statistics by a factor of ~ 2.5 in the mass region above 1600 MeV by adding a trigger which used larger solid-angle forward scintillation counters, and required two central tracks in the drift chamber with $p_T \gtrsim 600$ MeV/c. The exclusive $\pi^+\pi^-$ spectrum for this additional sample, after correcting for acceptance differences, is consistent with that of Fig. 6c and they have been added together in Fig. 6d. The general shape is very similar to that of the dip–bump structure in the 1000–1600 MeV region, and it is not unreasonable to suspect that one or more higher mass resonances are also occurring here.

4.2 Acceptance calculation

The acceptance has been calculated using a DPE event generator, with uncorrelated scattered protons distributed as $\exp(-\alpha|t|)$, and a flat rapidity distribution ($|y| < 1$) of the central system. The relative acceptance is insensitive to the value of α, and the value of 6.5 GeV^{-2} which has been used is consistent with the data. The Monte Carlo events were passed through a detailed simulation of the central detector, producing pseudo-raw data tapes which were then analysed by the same program chain as for the data. The central rapidity distribution generated with S-wave decay of the central $\pi^+\pi^-$ system was then in satisfactory agreement with the data (Fig. 7). The calculated acceptance as a function of mass for S-wave decay is shown in Fig. 8.

4.3 The angular distributions

As part of our study of the $\pi^+\pi^-$ angular distributions we have examined the normalized moments of the D-functions [15]. The coordinate system was chosen so that the z-axis lies along the t-channel axis in the $\pi^+\pi^-$ rest frame (i.e. the **PP** direction) with the y-axis perpendicular to the **PP** $\rightarrow (\pi\pi)$ production plane in the pp c.m. system. The angles (θ, ϕ) describe the π^+ direction in the $\pi^+\pi^-$ rest frame. The normalized moments are defined by [15]:

$$\langle D^L_{M0} \rangle = H(LM) = (1/N) \sum_{i=1}^{N} D^L_{M0}(\phi_i, \theta_i, 0),$$

where

$$D^L_{M0}(\phi,\theta,0) = \sqrt{[4\pi/(2L+1)]}\, Y^{L*}_M(\theta,\phi),$$

and N is the number of events in a given mass bin. The interaction is symmetric for $\theta \rightarrow \pi - \theta$ or $\phi \rightarrow -\phi$, implying that all moments are real, and only non-zero for L + M = even. All moments up to and including L = M = 6 were investigated, and those which showed significant deviations from pure S-wave behaviour are shown in Fig. 9, together with a line showing the expected behaviour for pure S-wave.

There is a localized effect at the ϱ^0 mass in Re H(11) and Re H(31), which can be explained by a small amount of ϱ^0 in the data, only visible in interference terms and negligible in the cross-section. The moments H(20), Re H(22), and H(40), although non-zero, are clearly as expected for an S-wave below 1000 MeV. The data are thus dominated by the S-wave at low mass. There are small discrepancies for $M(\pi\pi) \lesssim 0.5$ GeV in H(20) and H(40), which we ascribe to inaccurate Monte Carlo simulation of very low momentum tracks, causing the D-wave behaviour of the drift-chamber response to be overestimated. In the 1100 to 1500 MeV region, H(20) and H(40) show that some D-wave is present. In the 1800 to 2400 MeV range the data are consistent with being mostly D-wave; the dashed curve in Fig. 9e shows the Monte Carlo prediction for H(40) for a pure D-wave (m = 0). The moment Re H(22) exhibits significant structure in the region 1050–1500 MeV but similar effects are not observed in Re H(42) and Re H(44), and therefore the m = 2 state contributes little to the cross-section. The behaviour of H(60) above 1800 MeV is evidence for some G-wave (J = 4) in this region.

The dominance of the S-wave at low mass is evident without further analysis. Morgan and Pennington [16] have fitted an early sample of our data [1] to a model of the **PP** $\to \pi^+\pi^-$ subprocess, dominated by the final-state elastic $\pi\pi$ interaction. This provides an accurate description of our data below 1150 MeV and shows that no resonances other than S*(980) and ϵ(1300) are found in the S-wave. In order to understand the behaviour at higher mass we have performed a partial-wave analysis.

4.4 Partial-wave analysis

The $\pi^+\pi^-$ exclusive events have been fitted to a simple DPE model. This allows only the J^{PC} values 0^{++}, 2^{++}, 4^{++}, etc., and population of only the m = 0 magnetic substate. The G-wave (J = 4) is not expected to be significant below a mass of 2 GeV. The only contributions are then from S-wave and D-wave (m = 0). The angular distribution I(cos θ) is parametrized in terms of the density matrix elements $\varrho^{j_1 j_2}_{m_1 m_2}$ [17]:

$$2I(\cos\theta)/N = \varrho^{00}_{00} + 2\sqrt{5}\varrho^{20}_{00} D^2_{00}(\cos\theta) + 5\,\varrho^{22}_{00}[D^2_{00}(\cos\theta)]^2,$$

where

$$0 \le \varrho^{00}_{00} \le 1, \qquad \varrho^{00}_{00} + \varrho^{22}_{00} = 1$$

and

$$|\varrho^{20}_{00}|^2 \le |\varrho^{00}_{00}|\,|\varrho^{22}_{00}|.$$

(Here ϱ^{20}_{00} is taken to imply Re ϱ^{20}_{00}.)

The angular acceptance of the apparatus can be similarly expressed in terms of its moments G(LM):

$$2A(\cos\theta) = G(00) + 5G(20)\,D^2_{00}(\cos\theta) + 9G(40)\,D^4_{00}(\cos\theta),$$

where G(00) = 1.

The moments G(20) and G(40) are the Monte Carlo curves displayed in Fig. 9. A least-squares fit for the variables N, ϱ^{00}_{00}, and ϱ^{20}_{00} was performed to the corrected distributions, taking bins of 50 MeV in mass and 0.05 in $|\cos\theta|$, using the CERN program MINUIT [18]. The results are given in Table 1. A good fit was obtained in all bins except at 0.975 GeV where the S* causes large phase-shift variations within the bin. The results for ϱ^{00}_{00} and ϱ^{20}_{00} are plotted in Fig. 10 for the mass range 300 to 2300 MeV. The behaviour of ϱ^{00}_{00} confirms our previous conclusion that the data are dominated by the S-wave below 1100 MeV.

However, as previously mentioned, we observe a significant deviation from S-wave behaviour at low mass centred around 450 MeV, but we attach no physical significance to this effect.

The S- and D-wave cross-sections are given by

$$|S|^2 = N\varrho_{00}^{00}, \quad |D|^2 = N\varrho_{00}^{22},$$

after correction for relative acceptance as a function of mass. These are plotted in Fig. 11 for the mass range 1000 to 2300 MeV. A D-wave enhancement is evident, centred around 1350 MeV, and there is also a narrow effect of limited statistical significance at 1700 MeV. The high-mass continuum appears to be mostly D-wave, although no attempt has been made to extract the G-wave contribution in this region, owing to limited statistics.

4.5 Fit to S- and D-wave resonances

We have performed a simultaneous fit to the three distributions $|S|^2$, $|D|^2$, and ϱ_{00}^{20}, where

$$\varrho_{00}^{20} = \mathrm{Re}\, S^*D/(|S|^2 + |D|^2),$$

in the mass range 1000 to 2300 MeV. The S-wave amplitude was taken to be the sum of a fixed S*(975) (Γ = 33 MeV), a variable ϵ, and a coherent background of the form $Ae^{i\beta}/M$. In the D-wave amplitude the only state included at first was a fixed f(1270). The high-mass structure was parametrized in terms of an incoherent background of Gaussian form. The results of this fit are shown as dashed curves in Fig. 12. The overall χ^2/DF is 100/66 but the fit fails to reproduce the data for $|D|^2$ and ϱ_{00}^{20} in the mass range 1300 to 1700 MeV. There is no improvement if the f is replaced by a single variable D-wave object somewhat higher in mass. In the second fit an additional resonance was added coherently in the D-wave at around 1400 MeV (solid curves of Fig. 12). This provides an adequate description of the data (χ^2/DF = 64/62) and puts the extra state at 1480 ± 50 MeV with Γ = 150 ± 50 MeV. The dotted curves show the effect of adding a fixed θ(1700). This is consistent with the data (χ^2/DF = 55/60) although clearly not necessary in order to obtain a good fit. All fits put the scalar ϵ at 1420 MeV, somewhat higher than the currently accepted value of ~ 1300 MeV but in agreement with other recent studies [19]. Our 'θ' is at a similar level of significance to that observed by the Mark III Collaboration in the $\pi\pi$ decay channel [10]. The results are summarized in Table 2.

4.6 Cross-sections

The integrated luminosity for these data was about 30 pb^{-1}. We have estimated the differential cross-sections at our central t-value (given the assumptions described in Section 4.2). We quote the quantity

$$I = \int (d\sigma/dt_1 dt_2 dM)\, dM$$

for $t_1 = t_2 = -0.035$ GeV^2 and $|y| \leq 1$, in mass ranges corresponding to the main features in our mass spectrum:

I(S-wave) = 970 ± 410 μb GeV^{-4} for $M(\pi\pi) < 1$ GeV

I(S-wave) = 48 ± 20 μb GeV^{-4} for 1 GeV $\leq M(\pi\pi) <$ 1.6 GeV

I(S-wave) = 1.6 ± 0.8 μb GeV^{-4} for 1.6 GeV $\leq M(\pi\pi) <$ 2.3 GeV

I(D-wave) = $1.1^{+0.6}_{-0.5}$ μb GeV^{-4} for 1 GeV $\leq M(\pi\pi) <$ 1.6 GeV

I(D-wave) = 4.6 ± 1.9 μb GeV^{-4} for 1.6 GeV $\leq M(\pi\pi) <$ 2.3 GeV.

The quoted errors include systematic uncertainties conservatively estimated at 40%, the main source of which are the luminosity calibration, the value of the t slope α, and the Monte Carlo calculations.

4.7 Data at $\sqrt{s} = 45$ GeV

Some data were also obtained at $\sqrt{s} = 45$ GeV, the $|t|$ range of the forward protons being then shifted to $0.008 < |t| < 0.023$ GeV^2. The exclusive $\pi^+\pi^-$ mass spectrum is shown in Fig. 13, with superimposed a smooth line corresponding to the $\sqrt{s} = 63$ GeV data, normalized to the same number of events. The shapes of the distributions are clearly indistinguishable.

5. OTHER EXCLUSIVE CHANNELS

5.1 K^+K^- exclusive events

The mass spectrum of the exclusive K^+K^- events is shown in Fig. 14a in 25 MeV bins. The observed threshold behaviour is consistent with the production of S*(980), but no $\phi(1020)$ is seen, again indicating that backgrounds from non-DPE are small. The spectrum above 1350 MeV is increasingly contaminated by particle misidentification and is therefore not presented.

The Monte Carlo acceptance for isotropic decay of the K^+K^- system is shown in Fig. 14b, where the dE/dx particle identification was approximately simulated. The acceptance has fallen to a small value at the θ mass, and any signal would be swamped by the background from pion events mentioned above. However, for K^+K^- masses from threshold up to 1350 MeV our sample is well identified. The data have been corrected for acceptance assuming a pure S-wave, and the result is plotted in Fig. 14c (only the statistical errors are shown). The peaked behaviour at threshold is probably a manifestation of the S*(980). We have estimated the cross-section in this mass range using the same method and assumptions as for the $\pi^+\pi^-$ events.

The integral

$$\int_{2M_k}^{1250\ \mathrm{MeV}} (d\sigma/dt_1 dt_2 dm)\, dm$$

for $t_1 = t_2 = -0.035$ GeV^2 and $|y| \leq 1$ is estimated to be $41 \pm 18\ \mu$b GeV^{-4}. We have also calculated the ratio $\sigma(K^+K^-)/\sigma(\pi^+\pi^-)$ (S-wave), shown in Fig. 14d. Although not constant (due presumably to resonance effects), it is of order unity in this mass range, demonstrating the flavour independence naïvely expected for DPE.

5.2 $p\bar{p}$ exclusive events

The effective mass distribution of the 64 exclusive $pp \to pp\bar{p}p$ events is shown in Fig. 14e (histogram). The Monte Carlo acceptance was calculated using the standard method and the corrected mass distribution is shown as the data points of Fig. 14e. We have estimated the cross-section $d^2\sigma/dt_1 dt_2$ for $t_1 = t_2 = -0.035$ GeV^2 and $|y| \leq 1$ to be $1.0 \pm 0.5\ \mu$b GeV^{-4}.

5.3 $\pi^+\pi^-\pi^+\pi^-$ exclusive events

Figure 15a shows the mass distribution of the 1774 four pion events. The events in this sample have four and only four charged tracks either identified unambiguously as pions or π/K ambiguous. From Σp_y and Σp_x distributions, as in the two (central) prong sample, we apply cuts and conclude that the non-exclusive background is negligible. From the small number (20) of identified $\pi^+\pi^-K^+K^-$ events we conclude that any misidentification background is also negligible. The solid line is the background obtained from mixed events. The procedure was to select four tracks at random from the sample, in the four-pion c.m. frame, and treat them as coming from one event. The mixed event curve does not follow the data in detail but we have not found any clear reason for the deviations. In particular there are no obvious effects corresponding to the opening of two-body channels (e.g. $\varrho^0\varrho^0$, S*S*, ff). A plot of one

$M(\pi^+\pi^-)$ as a function of the other $M(\pi^+\pi^-)$ (Fig. 15b, 2 entries per event) shows that no dominant two-body decay mode is present. However, there is some evidence for $\varrho^0\varrho^0$ production (about 15% of the data). This contrasts with the dominance of $\varrho^0\varrho^0$ in four-pion production in $\gamma\gamma$ collisions [20]. The mass spectrum of the events in the $\varrho^0\varrho^0$ region shows no significant structure. This can be compared with the enhancement observed around 1650 MeV by Mark III which favoured $J^P = 0^-$ [10], inaccessible in exclusive DPE. Likewise, we find no evidence for any $\pi^+\pi^+\pi^-$ or $\pi^-\pi^-\pi^+$ resonances in the data.

To search for possible resonance effects in the four-pion mass spectrum we have calculated various quantities which describe the event shape (e.g. thrust) and find no significant deviations, at any mass value, from an isotropic distribution. We thus find the data to be entirely constant with isotropic four-body phase-space production of the pions. The cross-section $d^2\sigma/dt_1dt_2$ for $t_1 = t_2 = -0.035$ GeV^2 and $|y| \leq 1$, where y is the rapidity of the 4π system, is estimated to be (80 ± 40) μb GeV^{-4}.

6. $\alpha\alpha \to \alpha\alpha\pi^+\pi^-$ EXCLUSIVE EVENTS

During the summer of 1983 a small sample of data was collected from a single ISR run with 63 GeV/c beams of α-particles. Pulse-height measurements from the forward trigger telescopes provided a means to reject events with α-particle breakup where one or more protons passed through the trigger counters. For about half of the data taking the discriminator thresholds were increased to accept only α-particles. Additional analog-to-digital converters (ADCs) measured the scintillator pulse heights to enable the final cuts to be made off-line (see below). Pulse-height measurements from the 12 drift chamber wires in each forward arm provided an additional check that the tracks had Q = 2. Figure 16 shows one of the trigger ADC spectra, with the cut which was applied. Background from one or two protons, or p + $^3_1$H, was effectively rejected but $^3_2$He would pass this cut.

After requiring two well-reconstructed forward tracks and two oppositely-charged central tracks of the standard quality we obtained 426 events. Figure 17a shows the central Σp_y distribution for the UP-UP trigger. The clear peak at ~ -0.52 GeV/c, taken with the mean forward vertical angle of 4.5 mrad, corresponds to a forward track momentum of $\sim$ 60 GeV/c. This establishes that the events are predominantly exclusive and that the forward particles are α-particles rather than $^3_2$He. Similarly, the DOWN-DOWN events have $\Sigma p_y \approx +0.52$ GeV/c. The events were all classified as $\pi^+\pi^-$, and the usual exclusive cuts were applied (see Fig. 18) leaving 195 events. The non-exclusive background is again estimated to be $\sim$ 5%.

The $\pi^+\pi^-$ effective mass distribution is shown in Fig. 19a. The acceptance was calculated in the same way as for the pp data, and in Fig. 19b the corrected data are shown (data points) with a line representing the pp $\sqrt{s} = 63$ GeV results (acceptance corrected) for the $\pi^+\pi^-$ S-wave. The two distributions are seen to have a similar shape.

We find that a value of the t-slope, α, of 15 ± 2 GeV^{-2} is consistent with the $\alpha\alpha$ data. We estimate the cross-section $d^2\sigma/dt_1dt_2$ for $t_1 = t_2 = -0.1$ GeV^2 and $|y| \leq 1$ to be 550 ± 250 μb GeV^{-4}. This result may be compared with that for pp $\to$ pp$\pi^+\pi^-$ if we convert both results to total cross-sections using the known t-dependence. This then gives

$$\sigma(\alpha\alpha \to \alpha\alpha\pi^+\pi^-;\ \sqrt{s} = 126\ \text{GeV})/\sigma(\text{pp} \to \text{pp}\pi^+\pi^-;\ \sqrt{s} = 63\ \text{GeV}) = 1.4 \pm 0.8.$$

We conclude that a sample of exclusive $\alpha\alpha \to \alpha\alpha\pi^+\pi^-$ events has been observed at $\sqrt{s} = 126$ GeV. A second ISR experiment [21] has also studied this process, albeit without reconstruction of the central system, and the cross-sections are in good agreement after allowing for the difference in the central rapidity acceptance. We remark that this is, in principle, a very clean channel for DPE, as only I = 0 exchange is allowed.

7 SUMMARY AND CONCLUSIONS

We have performed a study of central systems of charged particles produced in the DPE process, and in particular we have isolated high-purity samples of exclusive events with 2 or 4 central tracks. The major study has been of the $\pi^+\pi^-$ events. The mass spectrum shows order-of-magnitude drops in cross-section at 1.0 and around 1.5 GeV and further structure at higher mass. This behaviour is unlike that observed at the SFM where a strong f(1270) was observed [22], but the difference could be due to the different kinematic coverage of the experiments. The present experiment is at smaller |t| and the central rapidity is more restricted.

Analysis of the angular distributions has shown that the S-wave dominates up to a mass of 1.6 GeV. The S-wave data leave no room for additional scalar mesons with $\Gamma \gtrsim 10$ MeV besides S* and ϵ, and will provide valuable information on the $\pi\pi$ interaction, when combined with the results from other experiments [23]. We see no sign of the G(1590) which has been claimed in $\pi^-p \to \eta\eta n$. The D-wave shows a clear enhancement between 1200 MeV and 1500 MeV which cannot be fitted by f(1270) alone. In order to obtain a good overall fit to S- and D-wave amplitudes within the framework of the DPE model an additional state is needed, at $M = 1480 \pm 50$ MeV with $\Gamma = 150 \pm 50$ MeV. [The central mass and width both decrease somewhat if a $\theta(1700)$ is included; see Table 2.] One interpretation is that this new state is the orthogonal partner to the f(1270), 'f_T', resulting from the mixing of a 2^{++} glueball with a 2^{++} $q\bar{q}$ meson. Previous evidence for a state in this mass region has been seen in the K^+K^- and $K^0_sK^0_s$ channels from $\pi^-p \to K\bar{K}n$ [24] (M = 1410 to 1440 MeV).

Our partial-wave analysis of the $\pi^+\pi^-$ events shows some evidence for an additional narrow D-wave peak at 1.7 GeV. This could be due to the $\theta(1700)$, although the statistical significance is not strong. The Mark III Collaboration have recently reported similarly weak indications of the θ in the $\pi\pi$ channel [10]. The disappearance of the S-wave is evidently associated with the second sharp drop in our mass spectrum, the behaviour at higher mass being mostly D-wave. The shape of the spectrum in this region suggests resonant behaviour and it is likely that one or more broad states are present. Unfortunately, our particle identification did not extend to high enough momenta to investigate whether the θ (or f_T) is present in K^+K^- exclusive events. However, we measure the $K^+K^-:\pi^+\pi^-$ ratio to be $\sim$ 1 in the region from threshold up to 1250 MeV.

The $\pi^+\pi^-\pi^+\pi^-$ exclusive mass spectrum shows some structure but the data appear isotropic at all masses. Only a small proportion of the data is due to two-body decays ($\varrho^0\varrho^0$).

We conclude by commenting that our exclusive data show interesting behaviour in the $\pi^+\pi^-$ D-wave, but the production is dominated by the S-wave. Although the S*(980) reveals itself in a most striking manner, there is no evidence for any new 0^{++} states. The lack of a low-mass scalar glueball candidate poses a problem for some conventional models of the glueball spectrum.

We believe that this reaction mechanism is interesting not only for meson spectroscopy but also for investigating the mechanism of diffraction in high-energy hadron collisions. Given high enough c.m. energy the centrally-produced hadronic system appears to have properties which are independent of both $\sqrt{s}$ (45 GeV, 63 GeV, and 126 GeV) and the nature of the colliding hadrons (pp, $\alpha\alpha$). We conjecture that this apparent universality extends indefinitely in $\sqrt{s}$ and holds for any colliding hadrons, depending only on t_1, t_2, and the central rapidity acceptance.

We wish to thank the Research Councils in our home countries for their support and are grateful for the technical assistance of the experimental support group of the ISR at CERN. In particular, we thank the ISR operations group for the excellent running conditions.

REFERENCES

[1] T. Åkesson et al., Phys. Lett. **133B**, 268 (1983).

[2] R. Shankar, Nucl. Phys. **B70**, 168 (1974).
D.M. Chew and G.F. Chew, Phys. Lett. **53B**, 191 (1974).
D.M. Chew, Phys. Lett. **65B**, 367 (1976).
J. Pumplin and F.S. Henyey, Nucl. Phys. **B117**, 377 (1976).
B.R. Desai, B.C. Shen and M. Jacob, Nucl. Phys. **B142**, 258 (1978).
Y.M. Cho, Phys. Rev. Lett. **46**, 302 (1981)

[3] L. Baksay et al., Phys. Lett. **61B**, 89 (1976).
H. De Kerret et al., Phys. Lett. **68B**, 385 (1977).
D. Drijard et al., Nucl. Phys. **B143**, 61 (1978).
R. Waldi, K.R. Schubert and K. Winter, Z. Phys. **C18**, 301 (1983).

[4] V. Blobel et al., Nucl. Phys. **B69**, 237 (1974).
M. Della Negra et al., Phys. Lett. **65B**, 394 (1976).
J.C.M. Armitage et al., Phys. Lett. **82B**, 149 (1979).

[5] D. Robson, Nucl. Phys. **B130**, 328 (1977).

[6] R.L. Jaffe and K. Johnson, Phys. Lett. **60B**, 201 (1976).
J.F. Donoghue, K. Johnson and B.A. Li, Phys. Lett. **99B**, 416 (1981).

[7] V.A. Novikov et al., Nucl. Phys. **B191**, 301 (1981).
J.J. Coyne, P.M. Fishbane and S. Meshkov, Phys. Lett. **91B**, 259 (1980).
S. Minami, Lett. Nuovo Cimento **36**, 65 (1983).
I. Cohen, N. Isgur and H.J. Lipkin, Phys. Rev. Lett. **48**, 1074 (1982).
J.L. Rosner, Phys. Rev. **D 24**, 1347 (1981).
N.A. Tornqvist, Phys. Rev. **D 29**, 121 (1984).
H.J. Schnitzer, Nucl. Phys. **B 207**, 131 (1982).
J.F. Donoghue, Phys. Rev. **D 25**, 1875 (1982).

[8] F. Binon et al., Nuovo Cimento **A 78**, 313 (1983).

[9] C. Edwards et al., Phys. Rev. Lett. **48**, 458 (1982).
E.D. Bloom, Proc. 21st Int. Conf. on High-Energy Physics, Paris, 1982, J. Phys. **43**, Suppl. 12, C3-407 (1982).
W.S. Lockman, Proc. 18th Rencontre de Moriond, La Plagne, Savoie, 1983 (Ed. Frontières, Gif-sur-Yvette,1983), Vol. 1, p.469.

[10] D. Hitlin, Proc. 11th Int. Symposium on Lepton and Photon Interactions at High Energies, Ithaca, 1983 (Cornell Univ., Ithaca, 1983), p. 746.
K.F. Einsweiler, SLAC-REPORT-272 (May 1984).

[11] A. Etkin et al., Phys. Rev. Lett. **49**, 1620 (1982).
S.J. Lindenbaum, Proc. 18th Rencontre de Moriond, La Plagne, Savoie, 1983 (Ed. Frontières, Gif-sur-Yvette, 1983), Vol. 1, p. 441.

[12] H. Gordon et al., Nucl. Instrum. Methods **196**, 303 (1982).
O. Botner et al., Nucl. Instrum. Methods **196**, 315 (1982).

[13] M.G. Albrow et al., Nucl. Instrum. Methods **214**, 201 (1983).

[14] L. Rosselet, A calorimeter trigger system for the ISR Axial Field Spectrometer, Proc. Topical Conf. on the Application of Microprocessors to High-Energy Physics Experiments, CERN, 1981, CERN 81-07 (1981), p. 316.

[15] S.U. Chung, CERN 71-8 (1971).

[16] D. Morgan and M.R. Pennington, Phys. Lett. **137B**, 411 (1984).

[17] B.R. Martin, D. Morgan and G. Shaw, Pion-pion interactions in particle physics (Academic Press, London, 1976), Appendix B.

[18] F. James and M. Roos, CERN Computer Centre Long Write-up.
[19] D. Cohen et al., Phys. Rev. **D 22,** 2595 (1980).
A.C. Irving, A.D. Martin and P.J. Done, Z. Phys. **C10,** 45 (1981).
[20] Ch. Berger, Proc. 11th Int. Symposium on Lepton and Photon Interactions, Ithaca, 1983 (Cornell Univ., Ithaca, 1983), p. 376.
[21] V. Cavasinni et al., preprint CERN-EP/85-44 (1985).
[22] A. Palano et al., preprint CERN-EP/83-107 (1983).
A.M. Breakstone, Proc. 18th Rencontre de Moriond, La Plagne, Savoie, 1983 (Ed. Frontières, Gif-sur-Yvette, 1983), Vol. 1, p. 493.
[23] S.R. Sharpe, R.L. Jaffe and M.R. Pennington, Phys. Rev. **D 30,** 1013 (1984).
D. Morgan and M.R. Pennington (in preparation).
[24] H. Palka, Ph.D. Thesis, Univ. of Krakow (1983).
V. Chabaud et al., Nucl. Phys. **B223,** 1 (1983).

Table 1
Results from density matrix fitting

Mass (GeV)	ϱ_{00}^{00}	ϱ_{00}^{20}	N	χ^2/DF
0.325	$0.992^{+0.008}_{-0.022}$	$0.022^{+0.009}_{-0.009}$	4679 ± 75	1.27
0.375	$0.998^{+0.002}_{-0.019}$	$0.048^{+0.008}_{-0.008}$	6413 ± 90	0.99
0.425	$0.949^{+0.020}_{-0.019}$	$0.057^{+0.007}_{-0.007}$	7638 ± 110	0.81
0.475	$0.919^{+0.020}_{-0.020}$	$0.037^{+0.008}_{-0.008}$	7924 ± 121	0.57
0.525	$0.958^{+0.022}_{-0.021}$	$0.034^{+0.008}_{-0.008}$	7910 ± 133	1.02
0.575	$0.983^{+0.017}_{-0.024}$	$0.014^{+0.009}_{-0.010}$	7290 ± 136	1.20
0.625	$0.943^{+0.034}_{-0.033}$	$0.047^{+0.013}_{-0.014}$	6908 ± 205	1.17
0.675	$0.942^{+0.036}_{-0.035}$	$0.021^{+0.014}_{-0.015}$	6053 ± 188	0.27
0.725	$0.990^{+0.010}_{-0.037}$	$0.007^{+0.015}_{-0.015}$	5546 ± 170	1.86
0.775	$1.000^{+0.000}_{-0.017}$	$-0.008^{+0.012}_{-0.013}$	4774 ± 100	0.57
0.825	$1.000^{+0.000}_{-0.013}$	$-0.009^{+0.013}_{-0.013}$	4302 ± 95	1.24
0.875	$1.000^{+0.000}_{-0.009}$	$-0.028^{+0.013}_{-0.014}$	3971 ± 89	1.36
0.925	$1.000^{+0.000}_{-0.005}$	$-0.036^{+0.013}_{-0.014}$	3785 ± 84	2.13
0.975	$0.996^{+0.004}_{-0.005}$	$-0.069^{+0.016}_{-0.016}$	2655 ± 68	4.13

Table 1 (cont.)

Mass (GeV)	ϱ_{00}^{00}	ϱ_{00}^{20}	N	χ^2/DF
1.025	$0.991^{+0.005}_{-0.012}$	$0.097^{+0.022}_{-0.024}$	1035 ± 49	1.47
1.075	$0.999^{+0.001}_{-0.012}$	$0.041^{+0.032}_{-0.035}$	496 ± 32	2.75
1.125	$0.995^{+0.005}_{-0.012}$	$0.076^{+0.030}_{-0.033}$	540 ± 35	2.51
1.175	$0.995^{+0.005}_{-0.022}$	$-0.072^{+0.035}_{-0.038}$	553 ± 32	1.56
1.225	$0.994^{+0.005}_{-0.027}$	$-0.077^{+0.035}_{-0.037}$	607 ± 33	1.01
1.275	$0.967^{+0.013}_{-0.022}$	$-0.180^{+0.035}_{-0.037}$	561 ± 28	1.58
1.325	$0.956^{+0.014}_{-0.034}$	$-0.206^{+0.034}_{-0.036}$	596 ± 29	1.27
1.375	$0.925^{+0.021}_{-0.040}$	$-0.263^{+0.037}_{-0.038}$	508 ± 22	0.97
1.425	$0.949^{+0.018}_{-0.037}$	$-0.221^{+0.040}_{-0.042}$	444 ± 25	1.40
1.475	$0.991^{+0.008}_{-0.021}$	$-0.097^{+0.045}_{-0.048}$	326 ± 24	1.69
1.525	$0.997^{+0.003}_{-0.066}$	$0.051^{+0.055}_{-0.063}$	200 ± 22	0.61
1.575	$0.974^{+0.021}_{-0.185}$	$0.158^{+0.070}_{-0.090}$	100 ± 21	1.07
1.625	$0.965^{+0.030}_{-0.082}$	$0.184^{+0.078}_{-0.107}$	579 ± 13	1.63
1.675	$0.33^{+0.28}_{-0.19}$	$0.18^{+0.10}_{-0.22}$	48 ± 20	1.07

Table 1 (cont.)

Mass (GeV)	ϱ_{00}^{00}	ϱ_{00}^{20}	N	χ^2/DF
1.725	$0.13^{+0.19}_{-0.13}$	$-0.03^{+0.14}_{-0.25}$	59 ± 20	1.41
1.775	$0.87^{+0.14}_{-0.35}$	$0.03^{+0.16}_{-0.25}$	40 ± 20	0.66
1.825	$0.61^{+0.30}_{-0.30}$	$-0.08^{+0.18}_{-0.26}$	46 ± 21	0.71
1.875	$0.27^{+0.36}_{-0.24}$	$-0.25^{+0.25}_{-0.36}$	40 ± 20	0.62
1.925	$0.13^{+0.18}_{-0.13}$	$-0.03^{+0.13}_{-0.26}$	64 ± 22	1.43
1.975	$0.01^{+0.30}_{-0.01}$	$-0.07^{+0.20}_{-0.30}$	63 ± 22	0.74
2.025	$0.28^{+0.30}_{-0.21}$	$-0.28^{+0.22}_{-0.30}$	50 ± 20	0.48
2.075	$0.01^{+0.10}_{-0.01}$	$-0.08^{+0.13}_{-0.20}$	61 ± 19	0.83
2.125	$0.04^{+0.25}_{-0.04}$	$0.19^{+0.20}_{-0.30}$	39 ± 14	0.52
2.175	$0.17^{+0.29}_{-0.17}$	$-0.28^{+0.24}_{-0.30}$	45 ± 20	0.76
2.225	$0.07^{+0.17}_{-0.07}$	$0.02^{+0.12}_{-0.22}$	59 ± 20	1.60
2.275	$0.02^{+0.30}_{-0.02}$	$-0.15^{+0.22}_{-0.30}$	36 ± 20	1.31

Table 2

Results of fits to partial-wave amplitudes
(A11 masses and widths are in MeV. Amplitudes are in arbitrary units.
Phases are in radians relative to the f(1273).
Bold numerals indicate fixed quantities in fit.)

		Fit 1	Fit 2	Fit 3
S-wave	A	20 ± 3	20 ± 3	21 ± 3
	β	1.2 ± 0.1	1.6 ± 0.2	1.5 ± 0.2
	Mass	**975**	**975**	**975**
	Width	**33**	**33**	**33**
S*	Amplitude	1.7 ± 0.3	1.7 ± 0.3	1.8 ± 0.3
	Phase	4.0 ± 0.2	4.2 ± 0.2	4.2 ± 0.2
	Mass	1420 ± 20	1420 ± 20	1420 ± 20
	Width	440 ± 50	450 ± 50	460 ± 50
ϵ	Amplitude	5.2 ± 0.6	4.3 ± 0.7	4.4 ± 0.7
	Phase	5.1 ± 0.1	5.1 ± 0.2	5.0 ± 0.2
	Mass	**1273**	**1273**	**1273**
	Width	**179**	**179**	**179**
f	Amplitude	0.55 ± 0.04	0.60 ± 0.07	0.39 ± 0.06
	Phase	**0**	**0**	**0**
	Mass		1480 ± 50	1410 ± 50
	Width		150 ± 40	80 ± 40
X	Amplitude		0.35 ± 0.10	0.21 ± 0.10
	Phase		3.5 ± 0.3	1.8 ± 0.3
	Mass			**1700**
	Width			**120**
θ	Amplitude			0.29 ± 0.10
	Phase			4.1 ± 0.3
	χ^2/DF	100/66	64/62	55/60

Figure captions

Fig. 1 : A schematic side view of the apparatus. Only the right-hand forward detectors are shown; the apparatus is left–right symmetric.

Fig. 2 : The distribution of Σp_y (vertical momentum) for the UP–UP and DOWN–DOWN trigger configurations separately.

Fig. 3 : The truncated mean of the drift-chamber pulse height (dE/dx) as a function of $\log_{10}p$. a) two-prongs, b) four-prongs.

Fig. 4 : a) Σp_y (final state) $-$ Σp_y (initial state). The exclusive cut was applied at ± 80 MeV/c.
b) Σp_x (final state) $-$ Σp_x (initial state) after the Σp_y exclusive cut. The Σp_x exclusive cut was applied at $\pm$ 100 MeV/c.

Fig. 5 : The full $\pi^+\pi^-$ mass distribution (log scale). No correction for acceptance.

Fig. 6 : a) The low-mass end of the $\pi^+\pi^-$ mass spectrum, in 10 MeV bins ($\sim$ resolution).
b,c) The detail of the high-mass end of the $\pi^+\pi^-$ mass spectrum.
d) The high-mass end of the $\pi^+\pi^-$ mass spectrum after combining data from standard and high-mass triggers.

Fig. 7 : The rapidity distributions of the central $\pi^+\pi^-$ system in data (histogram) and Monte Carlo events (solid line).

Fig. 8 : The calculated acceptance as a function of mass for isotropic decay of the central $\pi^+\pi^-$ system.

Fig. 9 : Normalized D-moments of the $\pi^+\pi^-$ angular distributions as a function of $\pi^+\pi^-$ effective mass. The bin size is 25 MeV for $M < 1.6$ GeV and 50 MeV for $M \geq 1.6$ GeV. a) Re H(11). b) H(20). c) Re H(22). d) Re H(31). e) H(40). f) H(60). The solid line is the Monte Carlo prediction for a pure S-wave. The dashed line in (e) is for a pure D-wave (m = 0).

Fig. 10 : Density matrix elements, derived from the least squares fit. a) ϱ_{00}^{00}. b) ϱ_{00}^{20}.

Fig. 11 : The relative S- and D-wave cross-sections. a) $|S|^2$. b) $|D|^2$.

Fig. 12 : The fits to S- and D-wave amplitudes (see text).

Fig. 13 : The exclusive $\pi^+\pi^-$ mass spectrum from the $\sqrt{s} = 45$ GeV data. The solid line represents the $\sqrt{s} = 63$ GeV data, normalized to the same total number of events. No acceptance correction has been applied to either distribution.

Fig. 14 : a) The effective mass distribution of the K^+K^- exclusive events (no correction for acceptance).
b) The calculated acceptance for K^+K^- exclusive events as a function of K^+K^- mass. The kinematical effect of the particle identification cuts is shown.
c) The corrected K^+K^- mass spectrum.
d) The $K^+K^-/\pi^+\pi^-$ ratio as a function of mass.

e) The effective mass distribution of the $p\bar{p}$ exclusive events, uncorrected (histogram) and after correction for acceptance (points).

Fig. 15 : a) The effective mass distribution of the $\pi^+\pi^-\pi^+\pi^-$ exclusive events. No correction for acceptance. The line represents the data for mixed events (see text).
b) The larger $\pi^+\pi^-$ mass plotted against the smaller $\pi^+\pi^-$ mass for the $\pi^+\pi^-\pi^+\pi^-$ exclusive events (2 entries per event).

Fig. 16 : The scintillator pulse-height spectrum for one of the forward trigger counters in the $\alpha\alpha$ data. The Q = 1 peak at $\sim$ 1.5 units has been heavily suppressed by the trigger threshold.

Fig. 17 : The central Σp_y distributions in the $\alpha\alpha$ data, for the different trigger configurations.

Fig. 18 : The final exclusive cuts on the $\alpha\alpha$ data. The Σp_y cut was at ± 100 MeV/c and the Σp_x cut at ± 175 MeV/c.

Fig. 19 : a) The uncorrected $\pi^+\pi^-$ mass distribution for the $\alpha\alpha$ data, with the relative Monte Carlo acceptance indicated as a line.
b) The final corrected $\pi^+\pi^-$ mass distribution for the $\alpha\alpha$ data. The solid curve represents the acceptance-corrected $\sqrt{s}$ = 63 GeV pp $\rightarrow$ pp$\pi^+\pi^-$ S-wave data, normalized to the same number of events in $0.3 \leq M(\pi\pi) < 1.5$ GeV.

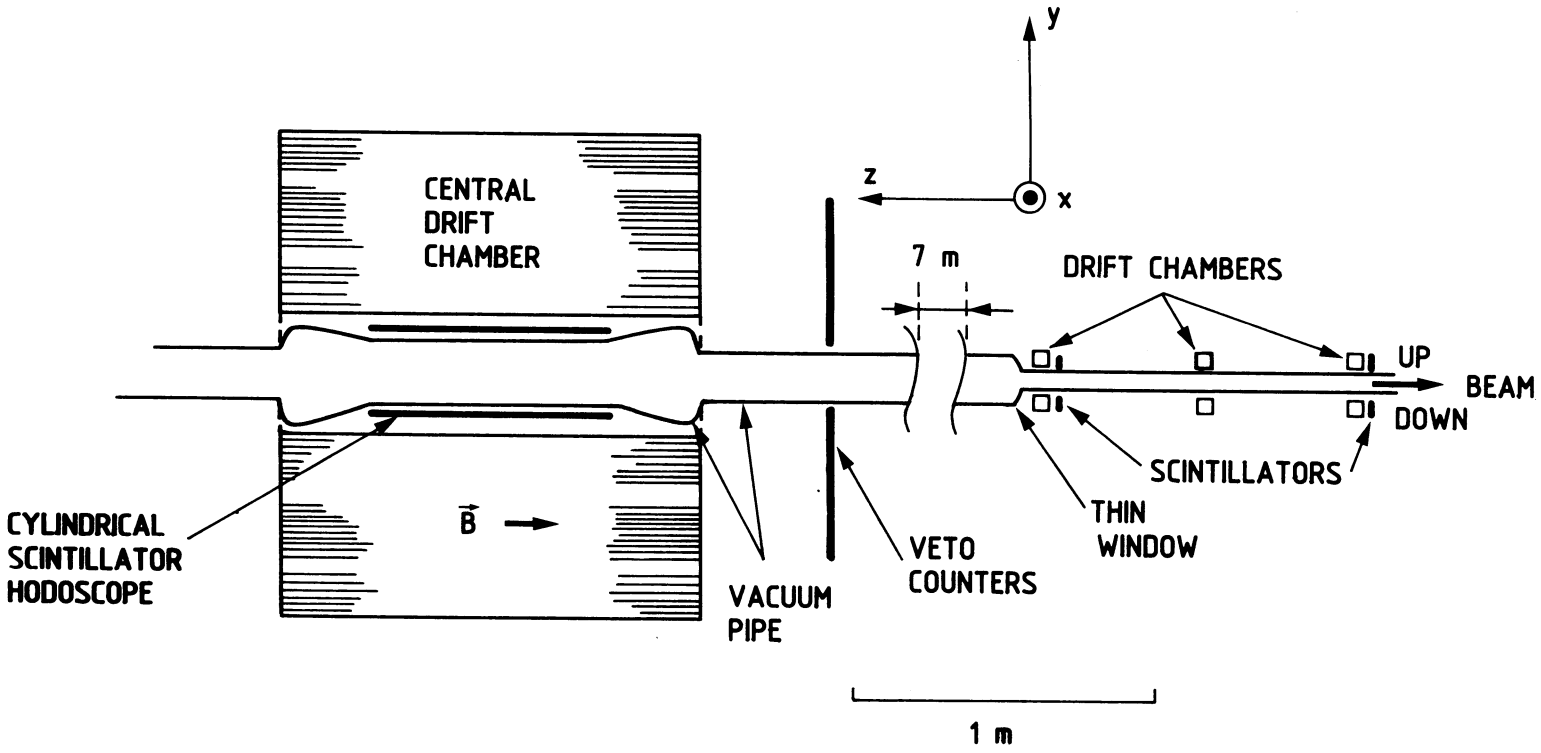
y
z
x
CENTRAL
DRIFT
CHAMBER
7 m
DRIFT CHAMBERS
UP
BEAM
DOWN
SCINTILLATORS
THIN
WINDOW
VETO
COUNTERS
VACUUM
PIPE
CYLINDRICAL
SCINTILLATOR
HODOSCOPE
B
1 m

Fig. 1

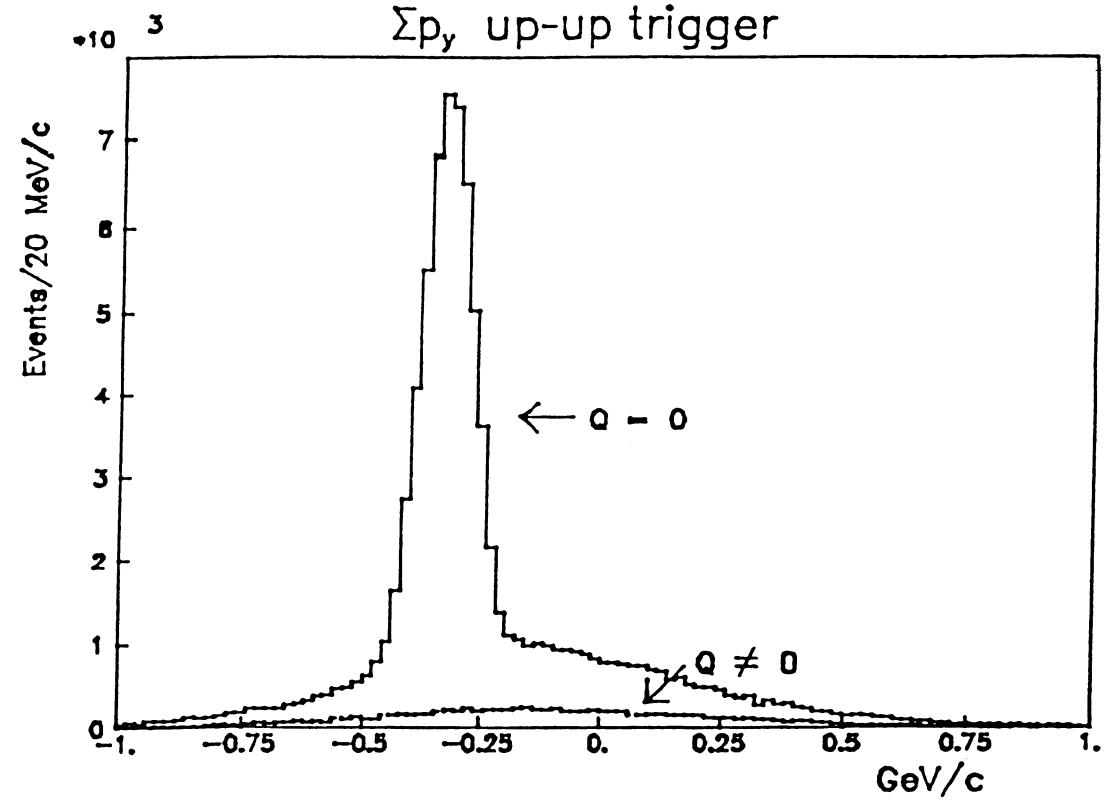
Σp_y up-up trigger
*10 3
Events/20 MeV/c
Q = 0
Q ≠ 0
GeV/c

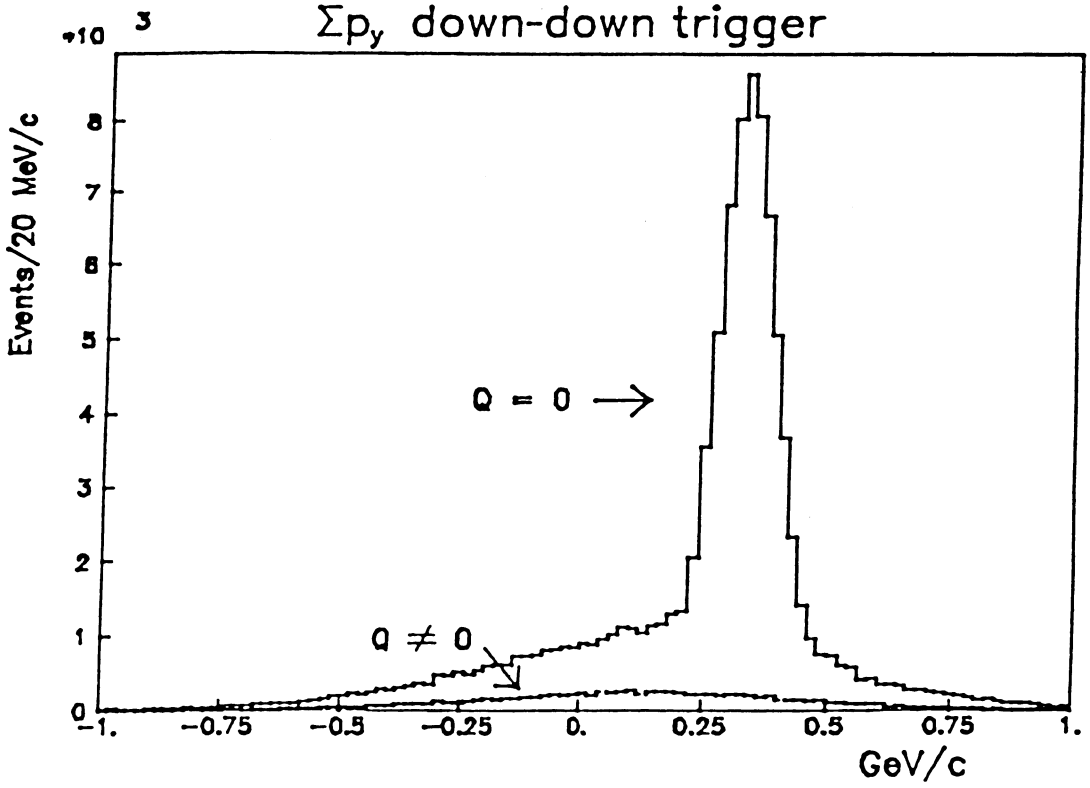
Σp_y down-down trigger
*10 3
Events/20 MeV/c
Q = 0
Q ≠ 0
GeV/c

Fig. 2

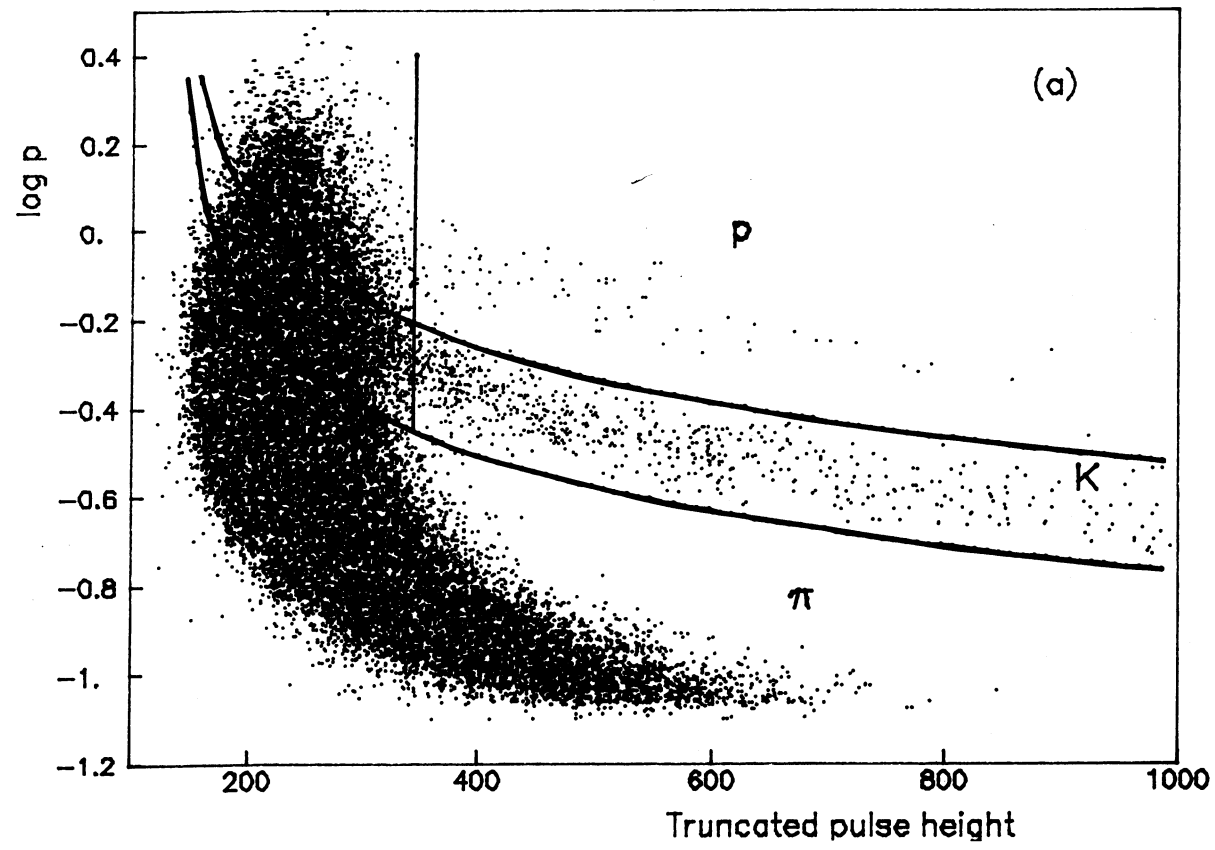
(a)
log p
0.4
0.2
0.
−0.2
−0.4
−0.6
−0.8
−1.
−1.2
p
K
π
200
400
600
800
1000
Truncated pulse height

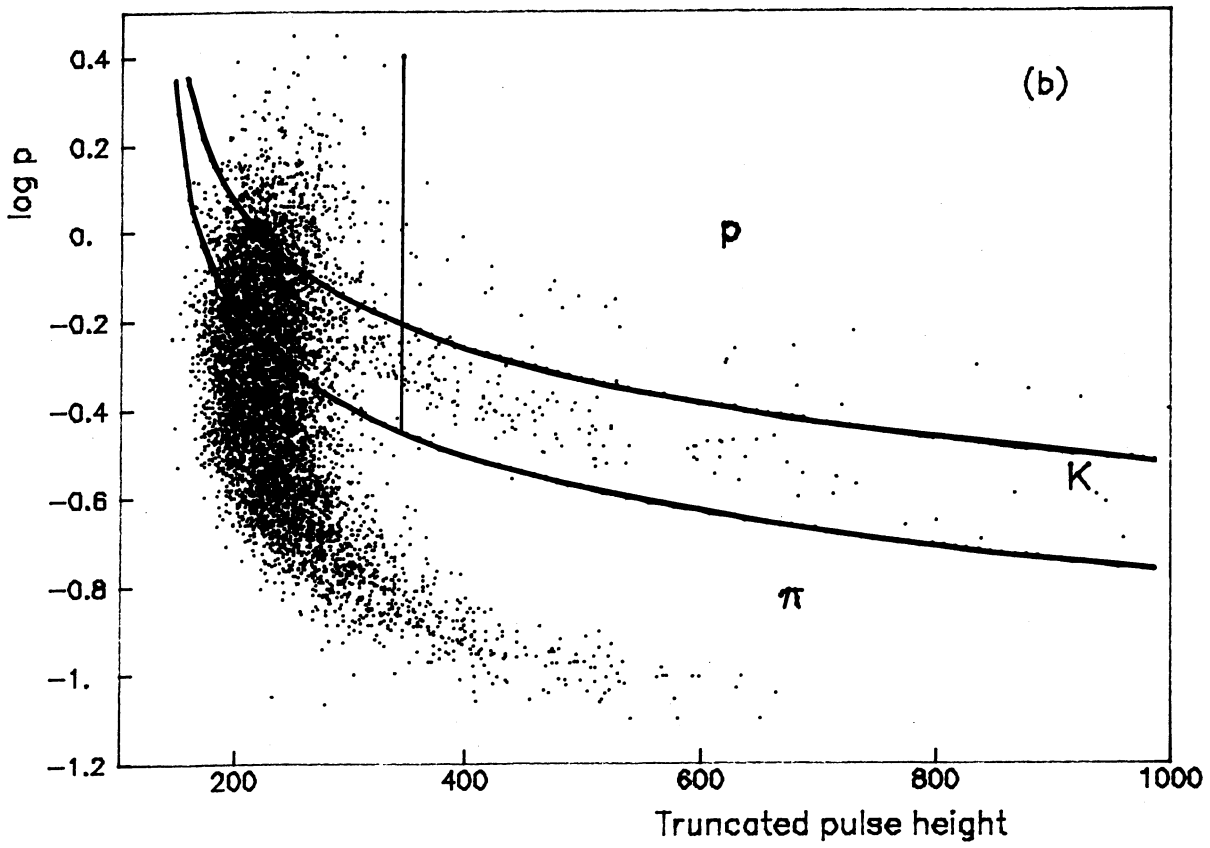
(b)
log p
0.4
0.2
0.
−0.2
−0.4
−0.6
−0.8
−1.
−1.2
p
K
π
200
400
600
800
1000
Truncated pulse height

Fig. 3

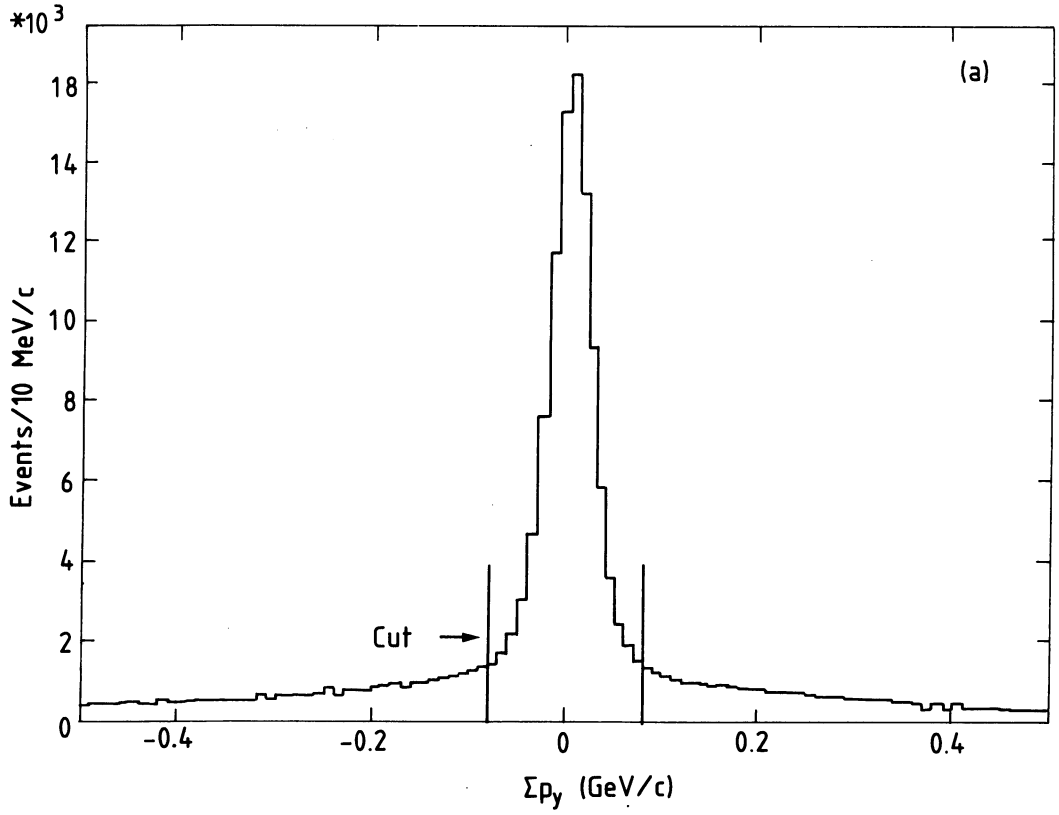
*10 3
(a)
Events/10 MeV/c
Cut
Σp_y (GeV/c)

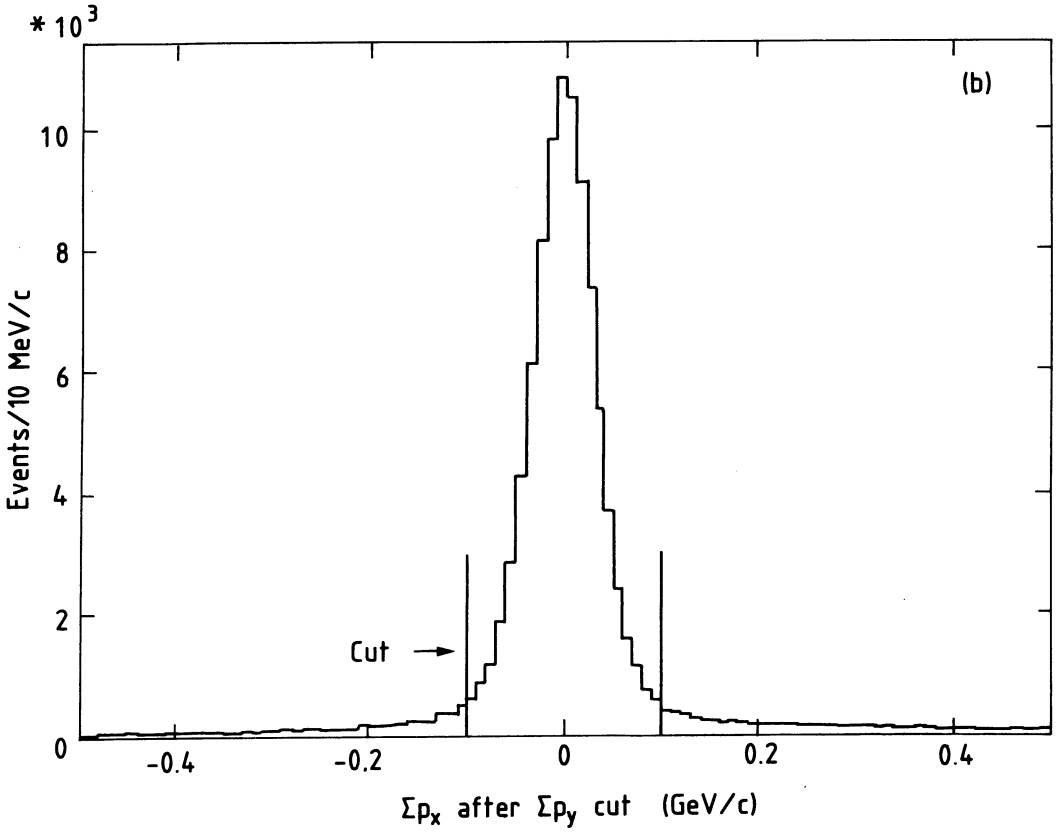
* 10 3
(b)
Events/10 MeV/c
Cut
Σp_x after Σp_y cut (GeV/c)

Fig. 4

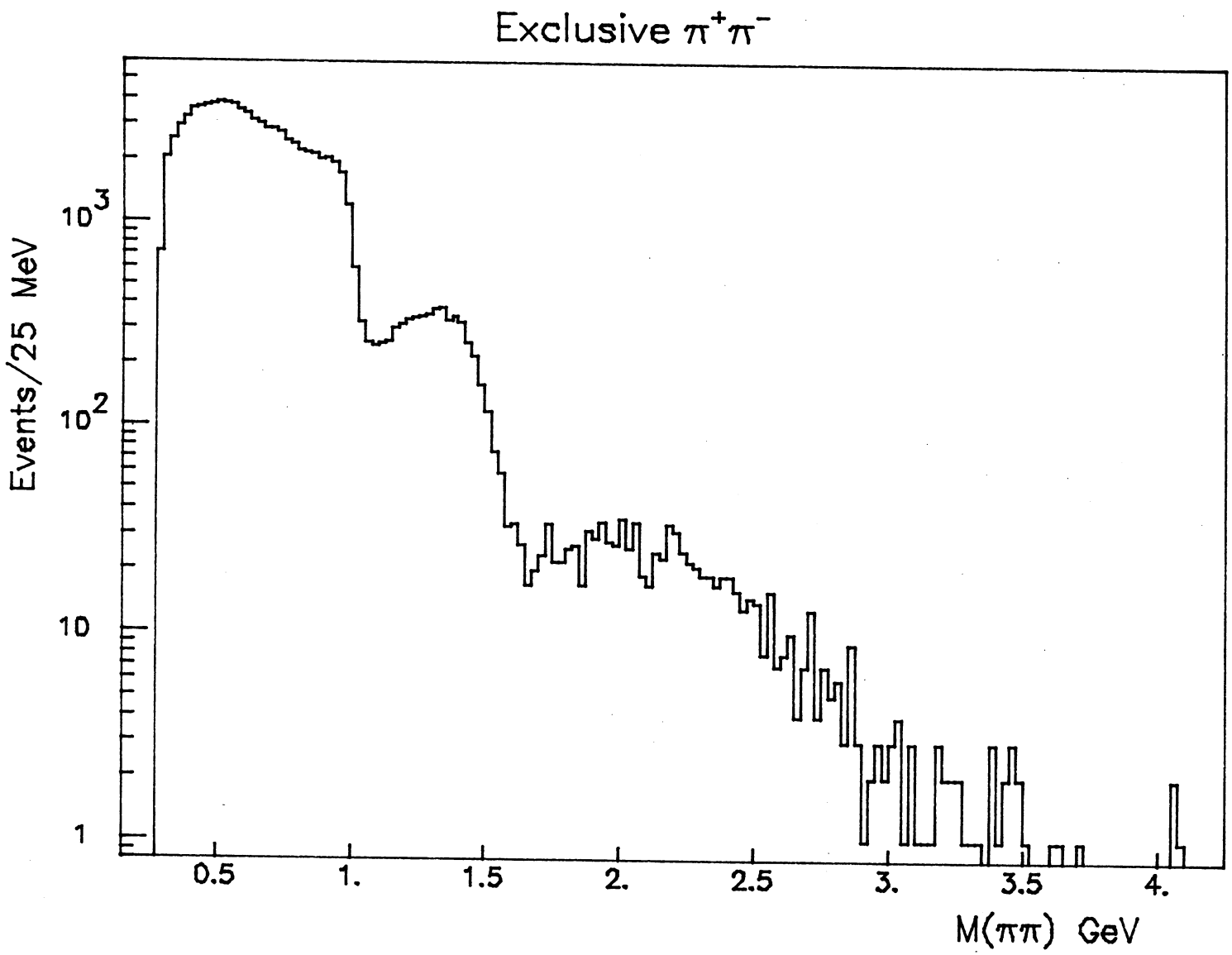
Exclusive $\pi^+\pi^-$
Events/25 MeV
10^3
10^2
10
1
0.5
1.
1.5
2.
2.5
3.
3.5
4.
M($\pi\pi$) GeV

Fig. 5

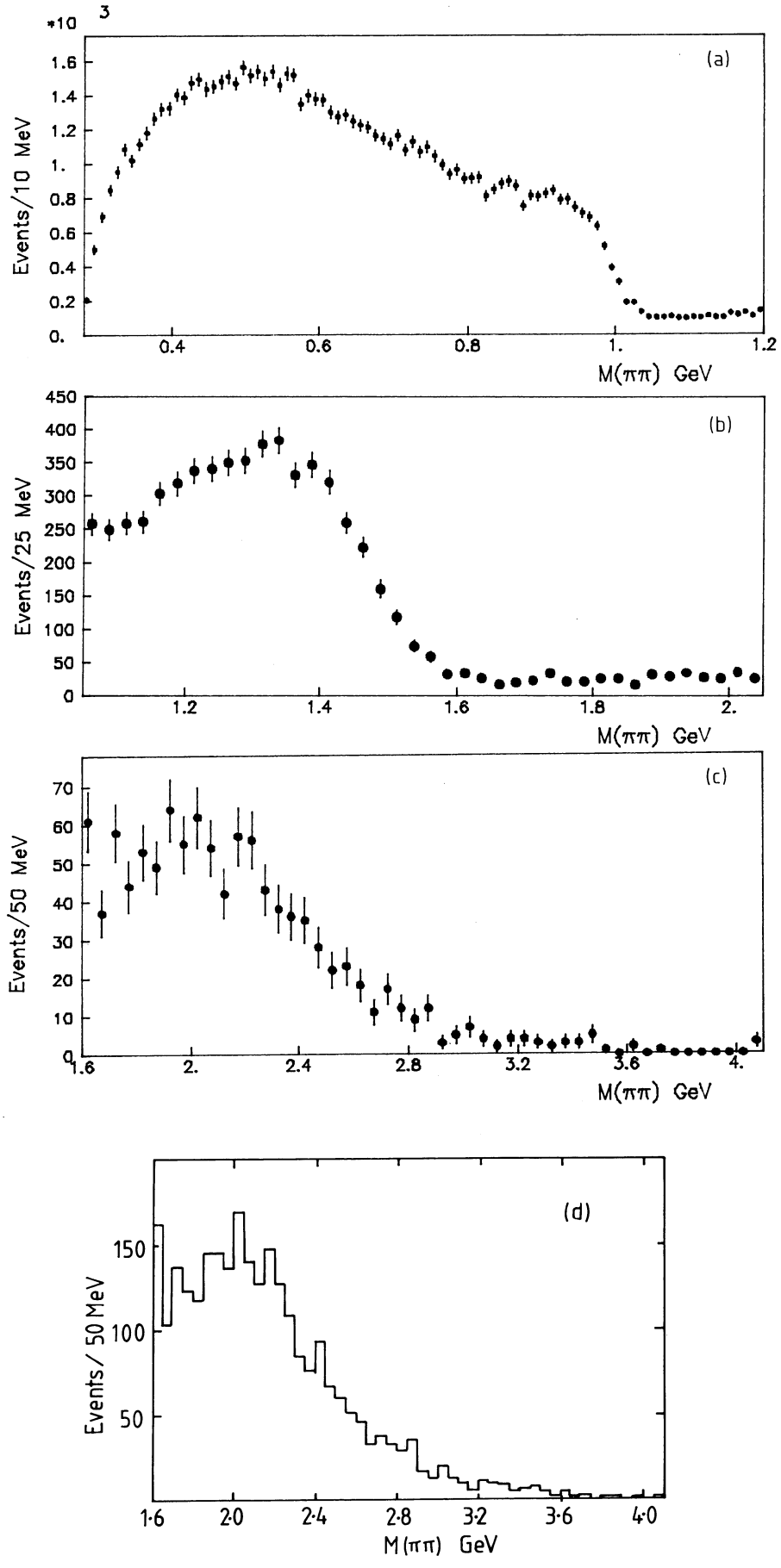
*10 3
(a)
Events/10 MeV
M(ππ) GeV
(b)
Events/25 MeV
M(ππ) GeV
(c)
Events/50 MeV
M(ππ) GeV
(d)
Events/ 50 MeV
M(ππ) GeV

Fig. 6

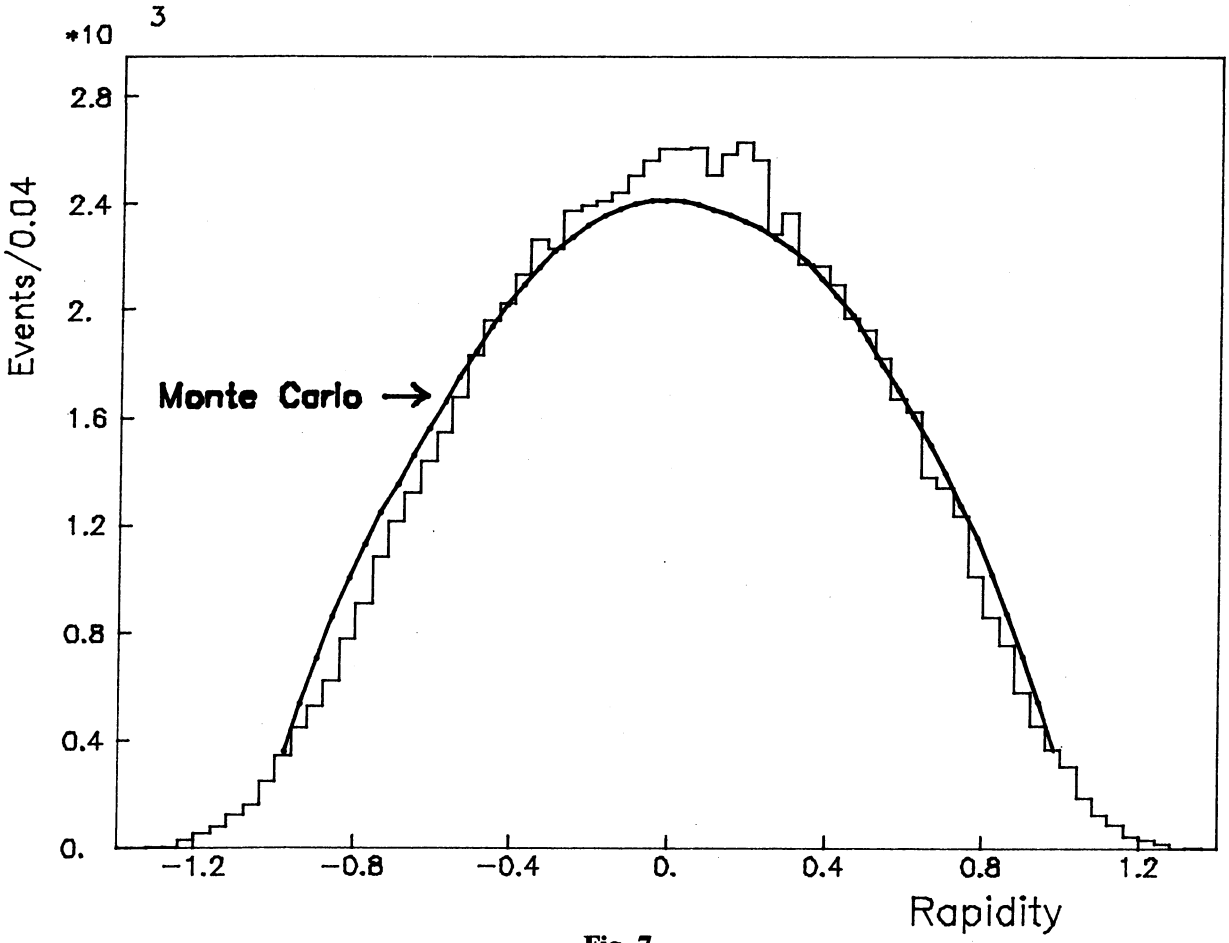
*10 3
2.8
2.4
2.
1.6
1.2
0.8
0.4
0.
Events/0.04
Monte Carlo →
−1.2
−0.8
−0.4
0.
0.4
0.8
1.2
Rapidity

Fig. 7

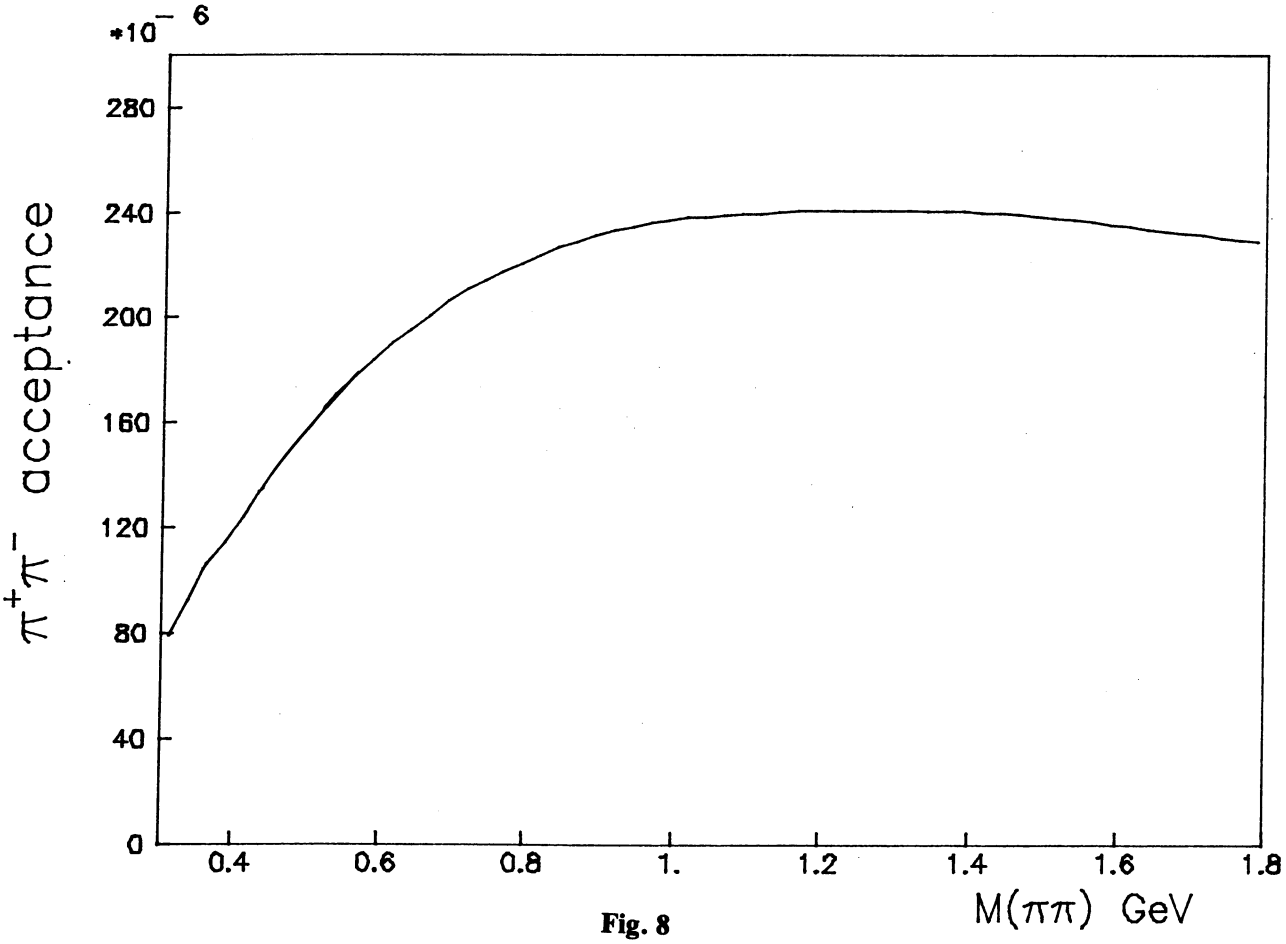
*10⁻ 6
280
240
200
160
120
80
40
0
π⁺π⁻ acceptance
0.4
0.6
0.8
1.
1.2
1.4
1.6
1.8
M(ππ) GeV

Fig. 8

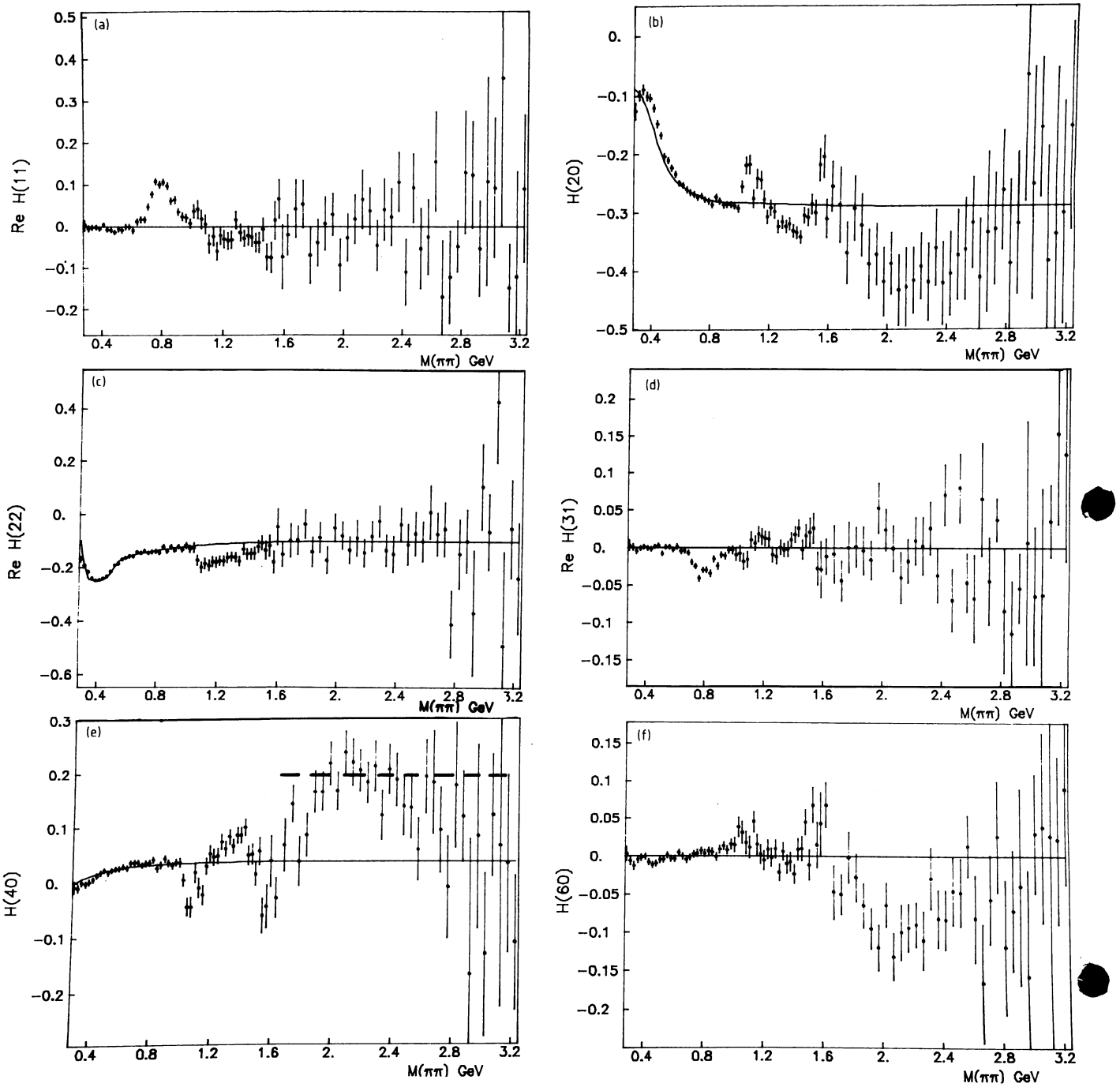
(a)
Re H(11)
M(ππ) GeV
(b)
H(20)
M(ππ) GeV
(c)
Re H(22)
M(ππ) GeV
(d)
Re H(31)
M(ππ) GeV
(e)
H(40)
M(ππ) GeV
(f)
H(60)
M(ππ) GeV

Fig. 9

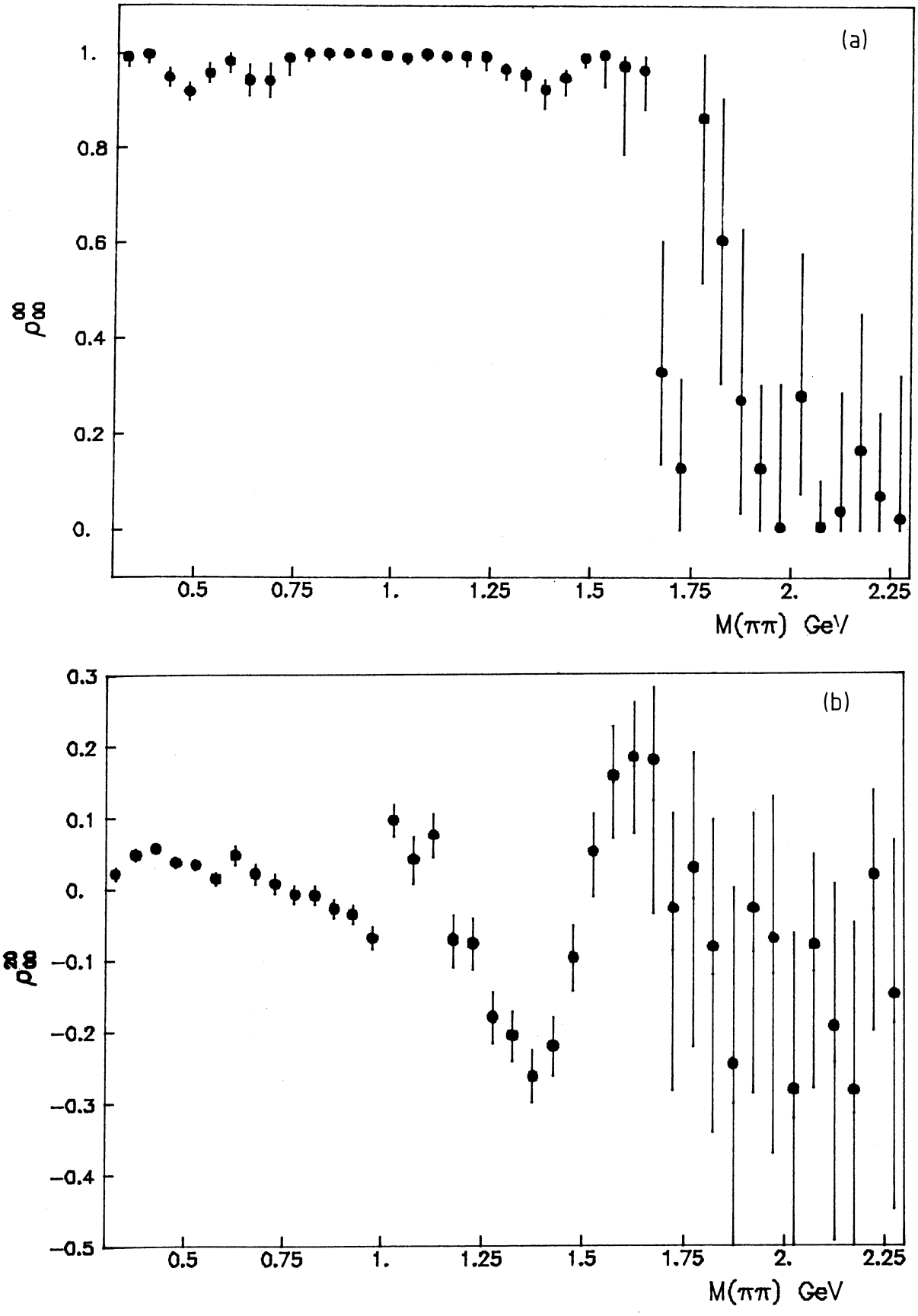
(a)
1.
0.8
0.6
0.4
0.2
0.
ρ_{88}
0.5
0.75
1.
1.25
1.5
1.75
2.
2.25
M(ππ) GeV
(b)
0.3
0.2
0.1
0.
−0.1
−0.2
−0.3
−0.4
−0.5
ρ_{88}
0.5
0.75
1.
1.25
1.5
1.75
2.
2.25
M(ππ) GeV

Fig. 10

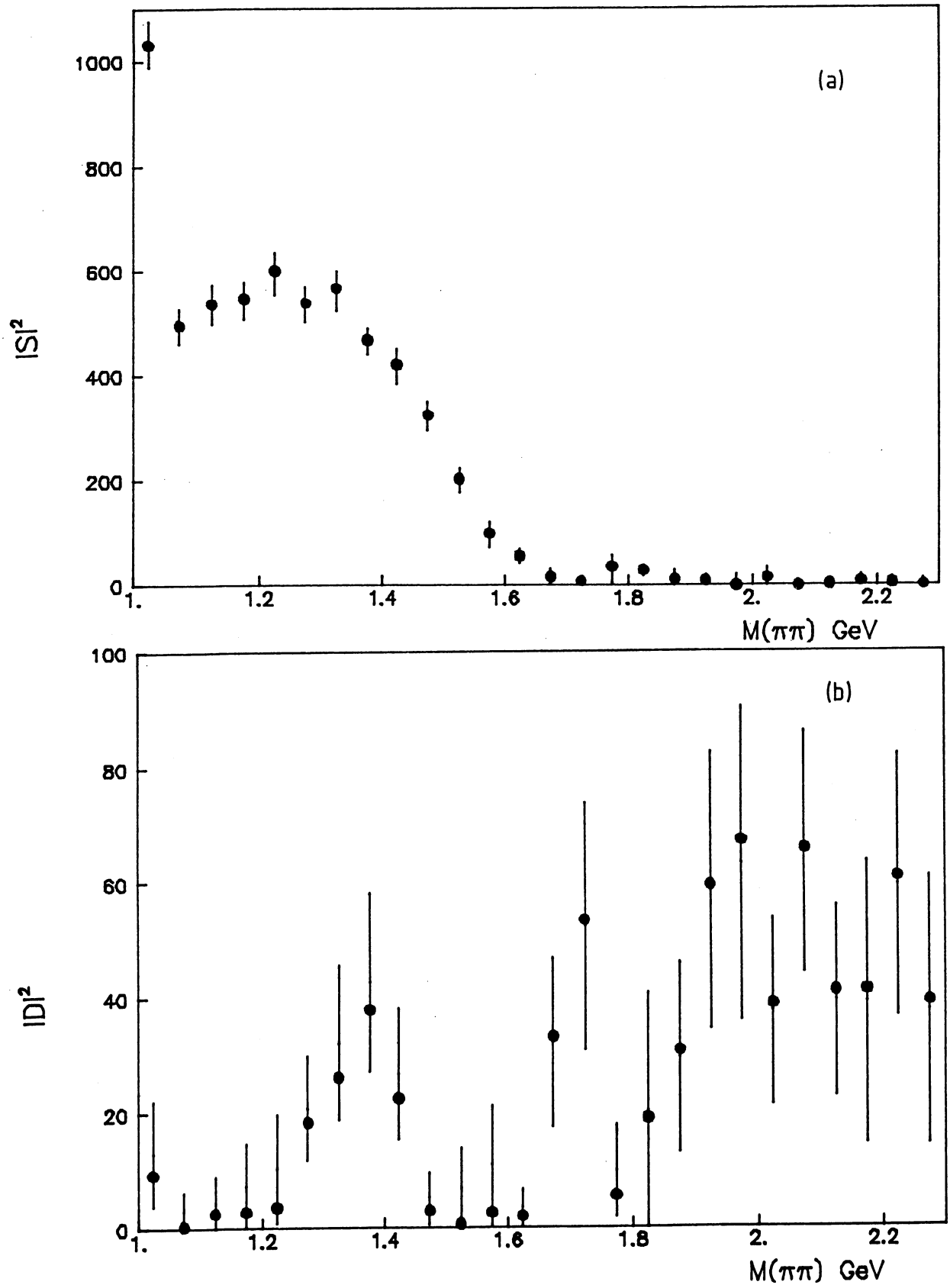
(a)
$|S|^2$
1000
800
600
400
200
0
1.
1.2
1.4
1.6
1.8
2.
2.2
M(ππ) GeV
(b)
$|D|^2$
100
80
60
40
20
0
1.
1.2
1.4
1.6
1.8
2.
2.2
M(ππ) GeV

Fig. 11

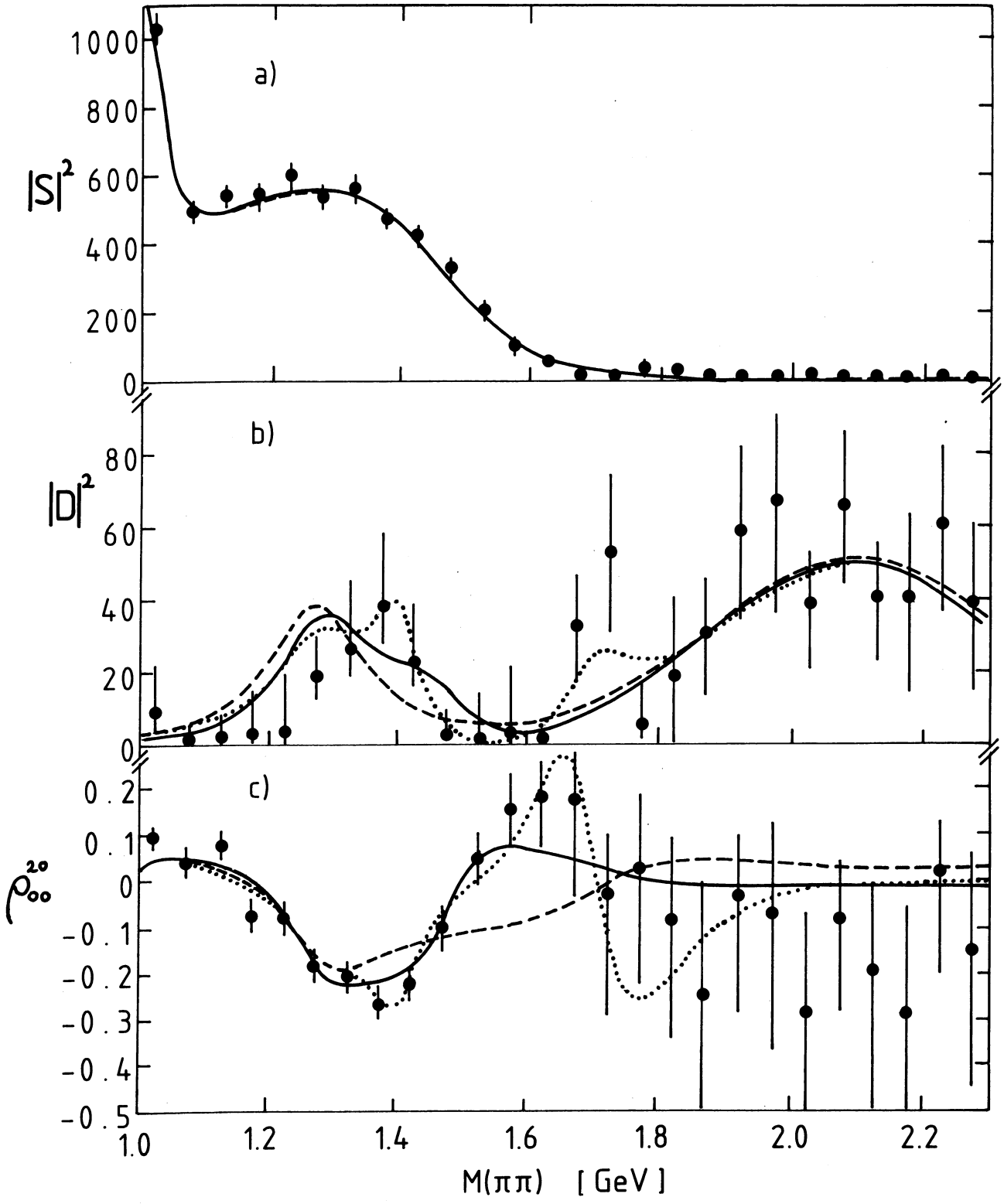
a)
b)
c)
$|S|^2$
$|D|^2$
ρ_{00}^{20}
1000
800
600
400
200
0
80
60
40
20
0
0.2
0.1
0
-0.1
-0.2
-0.3
-0.4
-0.5
1.0
1.2
1.4
1.6
1.8
2.0
2.2
M(ππ) [GeV]

Fig. 12

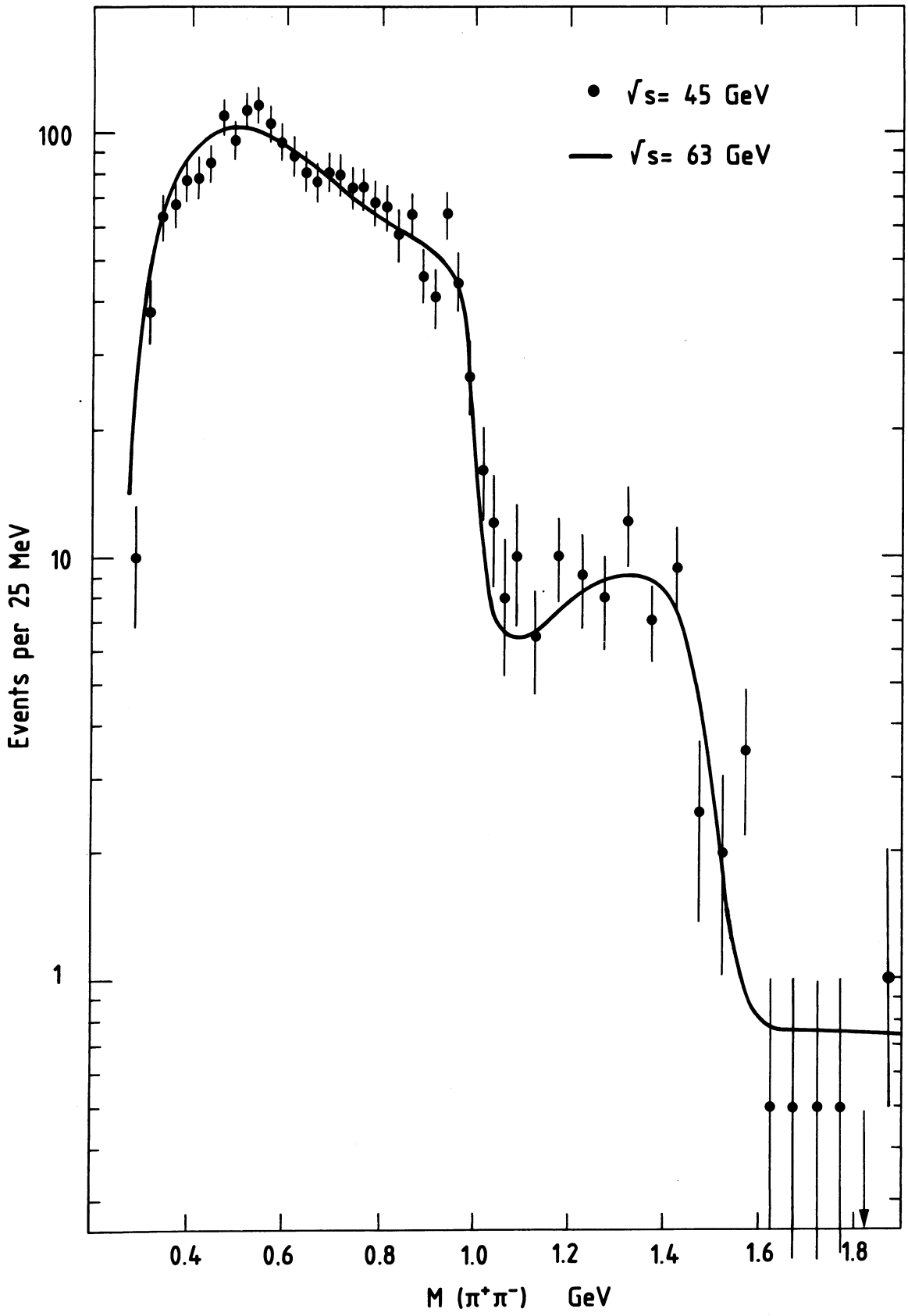
√s= 45 GeV
√s= 63 GeV
100
10
1
Events per 25 MeV
0.4
0.6
0.8
1.0
1.2
1.4
1.6
1.8
M (π⁺π⁻) GeV

Fig. 13

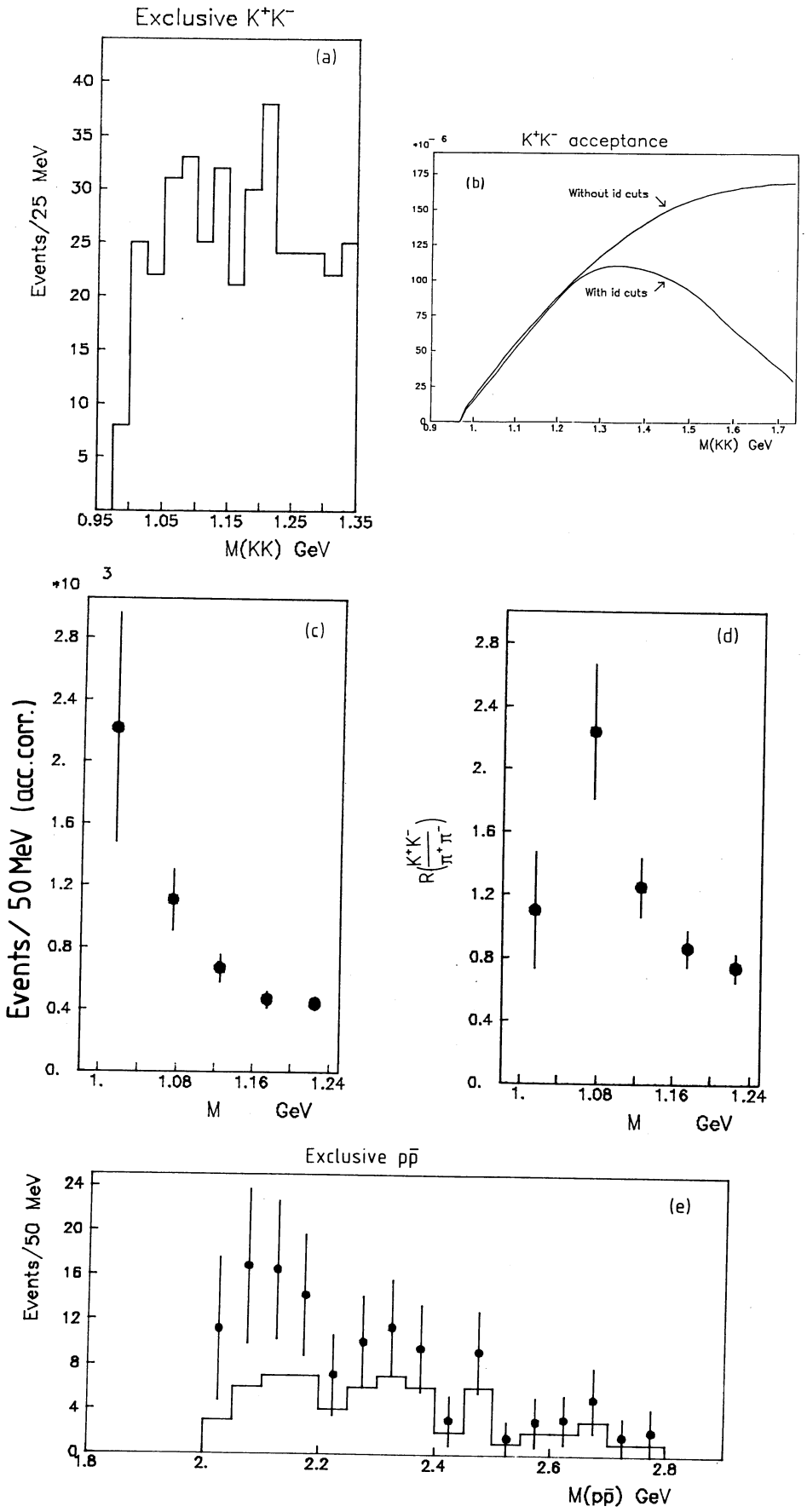
Exclusive K⁺K⁻
(a)
Events/25 MeV
M(KK) GeV
K⁺K⁻ acceptance
(b)
Without id cuts
With id cuts
M(KK) GeV
(c)
Events/ 50 MeV (acc.corr.)
M GeV
(d)
R(K⁺K⁻/π⁺π⁻)
M GeV
Exclusive pp̄
(e)
Events/50 MeV
M(pp̄) GeV

Fig. 14

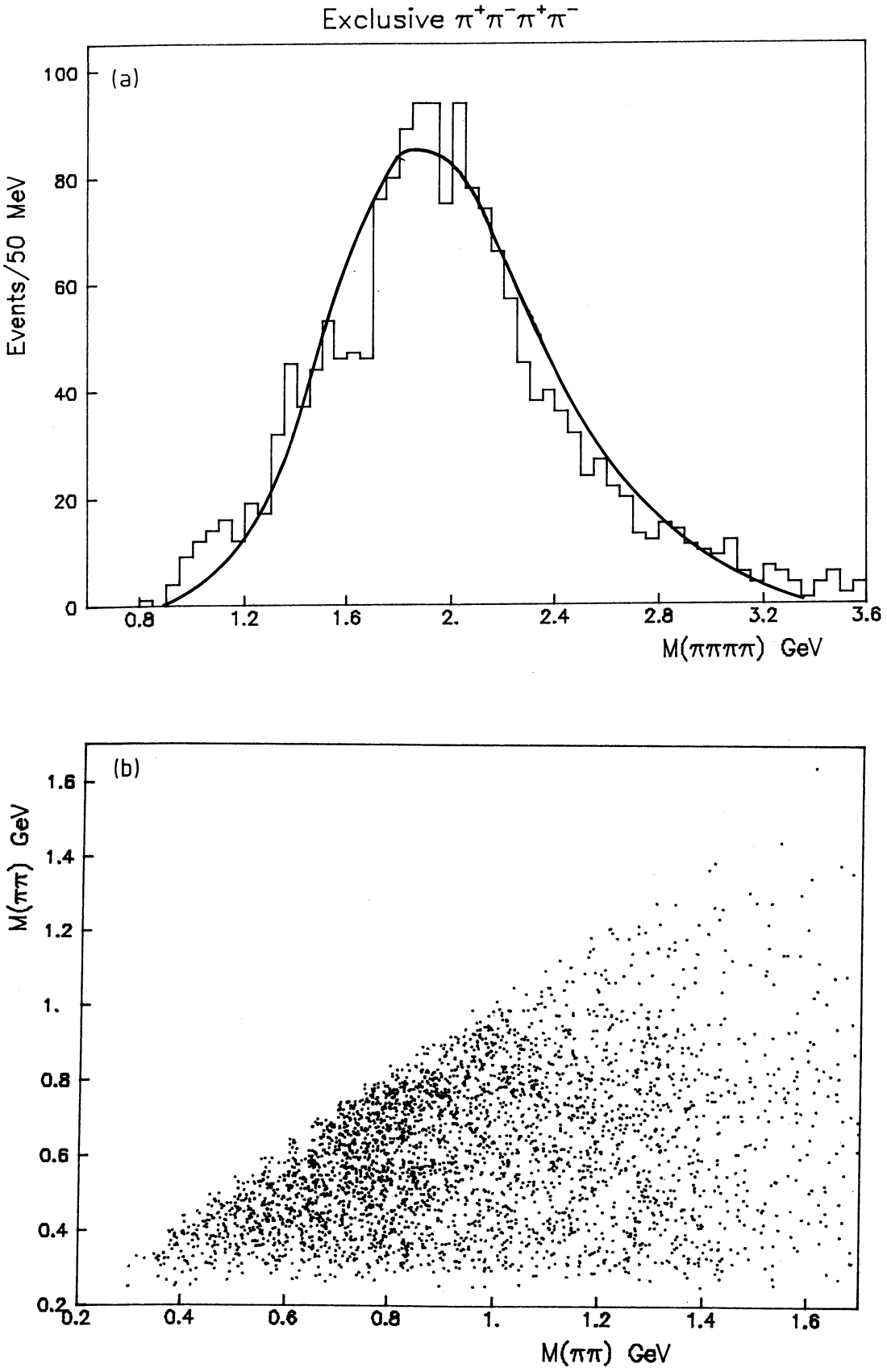
Exclusive $\pi^+\pi^-\pi^+\pi^-$
(a)
Events/50 MeV
100
80
60
40
20
0
0.8
1.2
1.6
2.
2.4
2.8
3.2
3.6
M(ππππ) GeV
(b)
M(ππ) GeV
1.6
1.4
1.2
1.
0.8
0.6
0.4
0.2
0.2
0.4
0.6
0.8
1.
1.2
1.4
1.6
M(ππ) GeV

Fig. 15

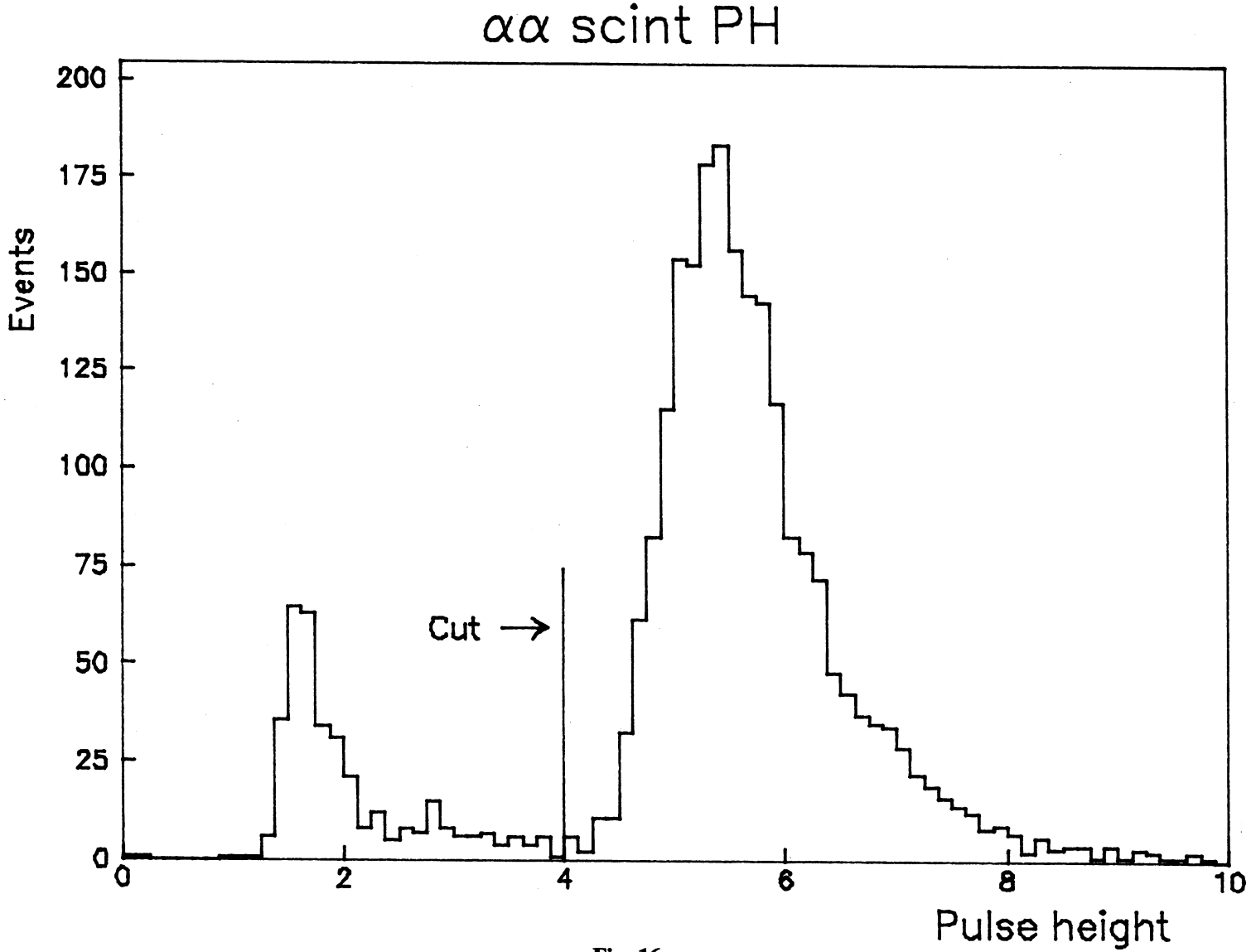
αα scint PH
Events
200
175
150
125
100
75
50
25
0
Cut
0
2
4
6
8
10
Pulse height

Fig. 16

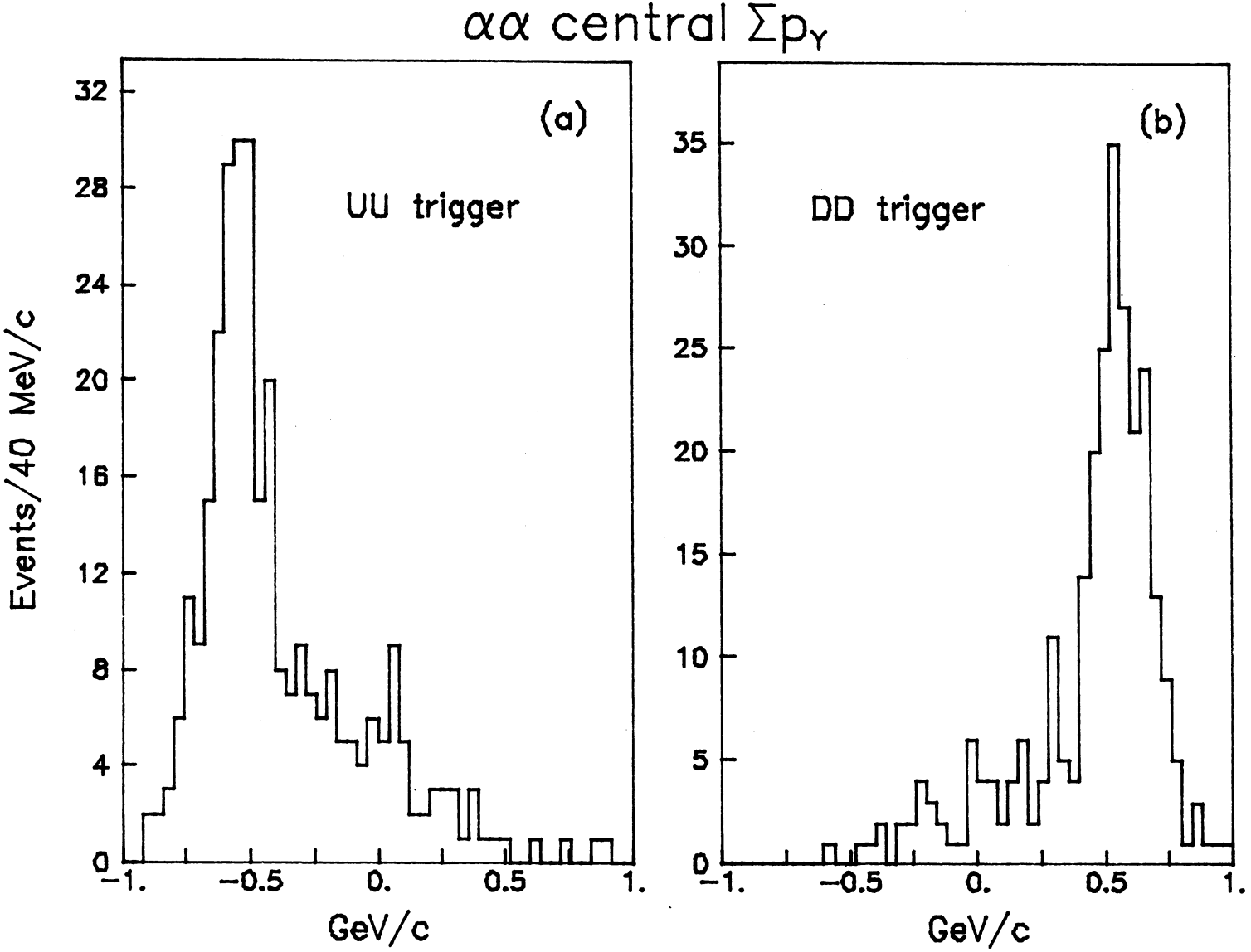
αα central Σp_Y
(a)
UU trigger
(b)
DD trigger
Events/40 MeV/c
GeV/c
GeV/c
0
4
8
12
16
20
24
28
32
0
5
10
15
20
25
30
35
−1.
−0.5
0.
0.5
1.

Fig. 17

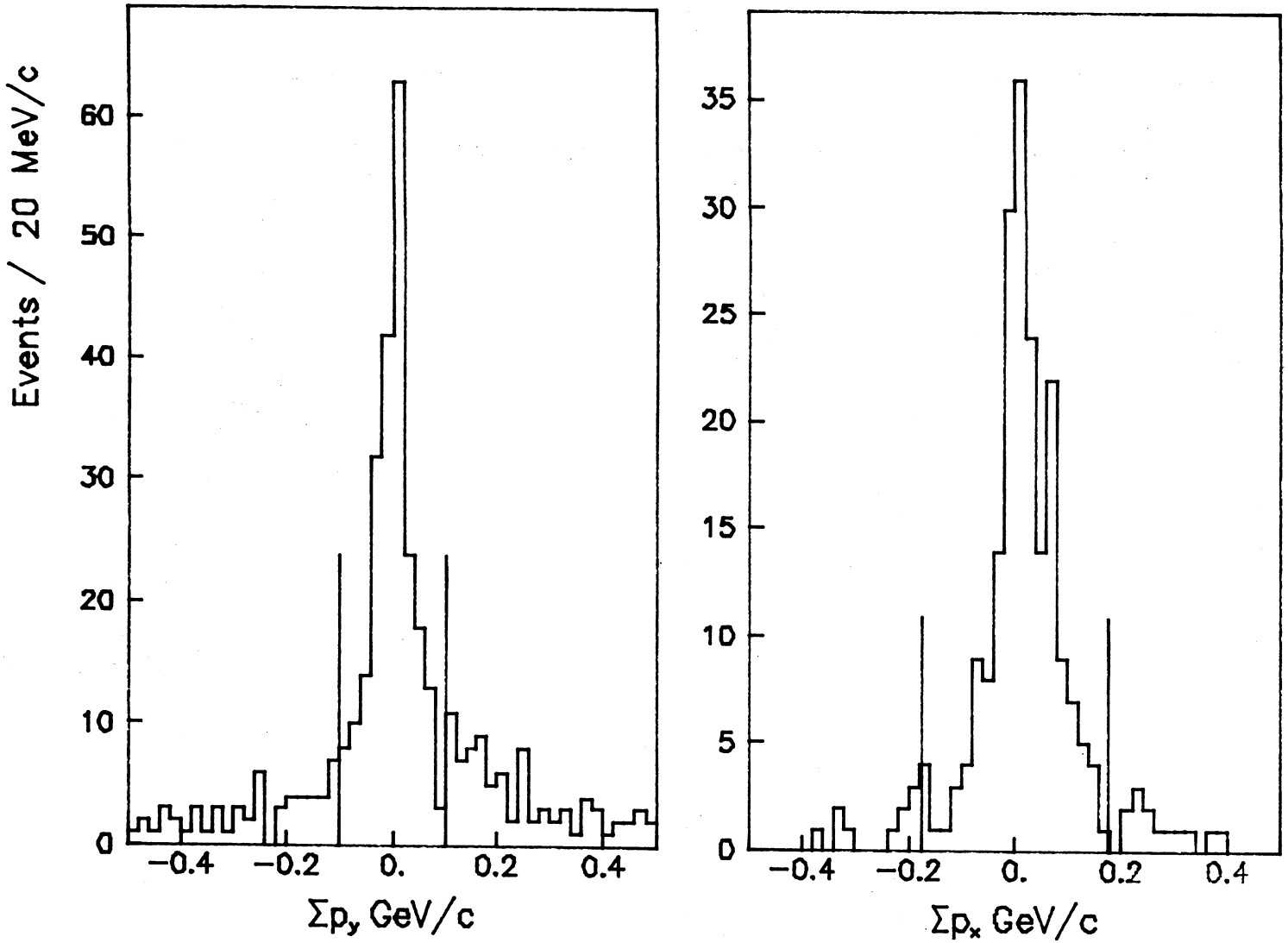
Events / 20 MeV/c
60
50
40
30
20
10
0
−0.4
−0.2
0.
0.2
0.4
Σp_y GeV/c
35
30
25
20
15
10
5
0
−0.4
−0.2
0.
0.2
0.4
Σp_x GeV/c

Fig. 18

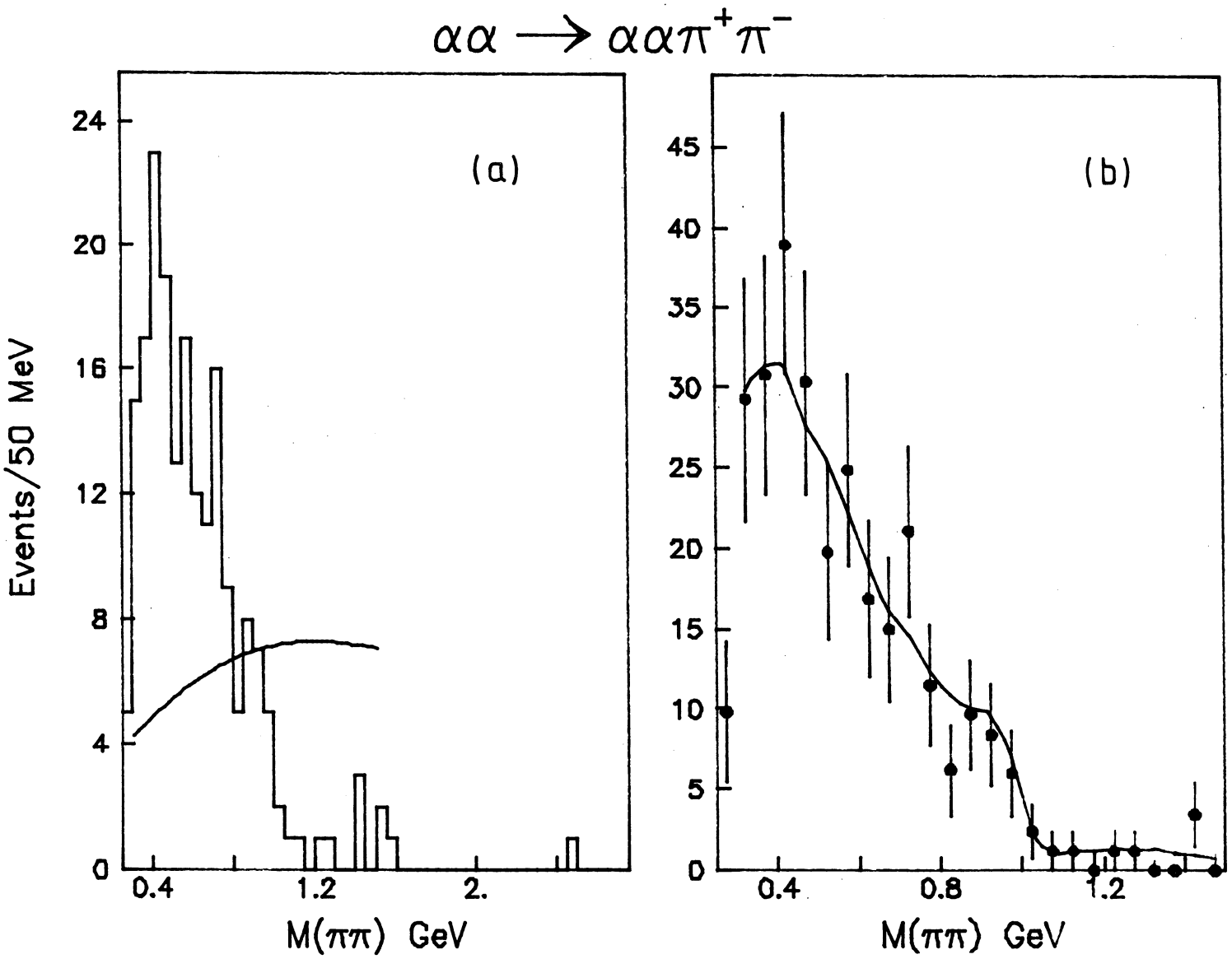
αα → ααπ⁺π⁻
(a)
(b)
Events/50 MeV
M(ππ) GeV
M(ππ) GeV
0
4
8
12
16
20
24
0
5
10
15
20
25
30
35
40
45
0.4
1.2
2.
0.4
0.8
1.2

Fig. 19